Plasma Mixing during active Kelvin-Helmholtz Instability under different IMF orientations

A. Settino[1], R. Nakamura[1], K. A. Blasl[1,2], D. B. Graham[3], T. K. M. Nakamura[1], O. W. Roberts[4], Z. Vörös[1,5], E. V. Panov[1], C. Simon Wedlund[1], D. Schmid[1], M. Hosner[1,2], M. Volwerk[1], Yu. V. Khotyaintsev[3]

[1]Space Research Institute, Austrian Academy of Sciences, Graz, Austria
[2]Swedish Institute of Space Physics, Box 537 SE–751 21 Uppsala, Sweden
[3]Universität Graz, Institut für Physik, Universitätsplatz 5, Graz, Austria
[4]Department of Physics, Aberystwyth, University, Aberystwyth, SY23 3BZ, UK
[5]Institute of Earth Physics and Space Science, HUN-REN, Sopron, Hungary

Key Points:

- Two Kelvin-Helmholtz events during northward and southward Interplanetary Magnetic Field orientations are compared using a mixing-parameter
- Higher mixing and local non-thermal features due to field-aligned ion beams during the northward Interplanetary Magnetic Field are observed
- Kinetic features of Kelvin-Helmholtz structures can identify both local and remote processes affecting the instability evolution

Corresponding author: Adriana Settino, `adriana.settino@oeaw.ac.at`

Abstract

When the velocity shear between the two plasmas separated by Earth's magnetopause is locally super-Alfvénic, the Kelvin-Helmholtz (KH) instability can develop. A crucial role is played by the interplanetary magnetic field (IMF) orientation, which can stabilize the velocity shear. Although, in a linear regime, the instability threshold is equally satisfied during both northward and southward IMF orientations, in-situ measurements show that KH instability is preferentially excited during the northward IMF orientation. We investigate this different behavior by means of a mixing parameter which we apply to two KH events to identify both boundaries and the center of waves/vortices. During the northward orientation, the waves/vortex boundaries have stronger electrons than ions mixing, while the opposite is observed at their center. During the southward orientation, instead, particle mixing is observed predominantly at the boundaries. In addition, stronger local ion and electron non-thermal features are observed during the northward than the southward IMF orientation. Specifically, ion distribution functions are more distorted, due to field-aligned beams, and electrons have a larger temperature anisotropy during the northward than the southward IMF orientation. The observed kinetic features provide an insight into both local and remote processes that affect the evolution of KH structures.

Plain Language Summary

Due to the velocity shear layer generated by the solar wind flowing past the Earth's magnetosphere, large surface Kelvin-Helmholtz (KH) waves and vortices can be formed at the magnetopause. These waves and vortices play a crucial role in transporting the solar wind particles through the magnetopause into the magnetosphere, where the particles form a so-called low-latitude boundary layer (LLBL). The particle transport occurs due to stretching and twisting of the magnetic field lines by the KH waves/vortices, which result in plasma mixing and diffusion through the magnetopause. It appears that spacecraft observe the KH waves/vortices more often during northward orientations of the interplanetary magnetic field (IMF). During northward IMF, the induced high-latitudes reconnection thicken the preexisting LLBL and lower the density gradient at the magnetopause, this favoring KH instability. Conversely, higher density jump and dayside reconnection, during southward IMF, can suppress the instability development and disrupt the KH vortices. To clarify these differences in the KH wave/vortex appearance under different IMF directions, we compare the wave/vortex and particle properties during both IMF orientations. We employ a mixing parameter, which helps identify specific regions of KH waves/vortices and investigate their kinetic signatures, thus providing an insight into KH evolution.

1 Introduction

The Kelvin-Helmholtz (KH) instability is a physical phenomenon which can develop in both fluids and plasmas when a velocity shear between two different interacting flows or within the same flow exists (Chandrasekhar, 1961; Miura, 1982). Its evolution typically results in the development of vortices that can eventually roll-up and merge. While fluids are KH-unstable for any amplitude of the jump velocity, in plasmas the magnetic field has a stabilizing effect. In particular, in the near-Earth environment, both numerical simulations and in-situ observations have shown that the instability is strongly affected by the velocity jump and the orientation of the solar wind magnetic field, resulting in a seasonal and diurnal variability of the KH growth rate (W. Y. Li et al., 2012; Nykyri, 2013; Kavosi et al., 2023). Moreover, in-situ measurements show that the KH instability at the low latitude magnetopause is most frequently observed during periods of northward IMF, when magnetic reconnection at the subsolar magnetopause tends to be suppressed (Kivelson & Chen, 1995; Fairfield et al., 2000; Nykyri & Otto, 2001; Nykyri et al., 2006; Hasegawa et al., 2004, 2006; Foullon et al., 2008; Kavosi & Raeder, 2015). In this case, the KH instability is believed to be mainly responsible for the efficient plasma transport and momentum transfer across the magnetopause boundary and for the formation of the low latitude boundary layer (LLBL), which is observed to be thickened on the magnetosphere side under northward IMF configurations (Fairfield et al., 2000; Otto & Fairfield, 2000; Nykyri & Dimmock, 2016; Henry et al., 2017; Nakamura, 2021). Indeed, during their non-linear evolution, KH vortices can highly twist and compress the magnetic field lines, thus generating thin current sheets which can eventually reconnect and contribute to locally generate a turbulent environment (Eriksson et al., 2016; W. Li et al., 2016; Stawarz et al., 2016; Sorriso-Valvo et al., 2019). This mechanism of vortex induced reconnection (VIR) can enhance particle mixing and favor the plasma entry across the magnetopause boundary (Daughton et al., 2014; Nakamura et al., 2017).

On the other hand, the KH instability is less likely to be observed during periods of southward IMF (Kavosi & Raeder, 2015). The first observation was reported by Hwang et al. (2012) that showed more fragmented and intermittent structures, contrary to the periodic signatures observed during northward IMF conditions. Such differences have been investigated in numerical simulations, showing the generation of competing mechanisms that stabilize the velocity shear and inhibit the growth of KH waves. For example, fully kinetic simulations showed that the development of the Rayleigh-Taylor instability can stretch KH vortices and prevent their rolling, thus destroying the periodicity and making their detection more difficult (Matsumoto & Hoshino, 2004; Faganello et al., 2008; Nakamura et al., 2022). Moreover, 3D fully kinetic simulations showed that VIR in multiple sites of the vortices can lead to a faster vortex decay (Nakamura et al., 2020). Furthermore, in configurations where the magnetic field changes its sign across the shear layer, magnetic reconnection, which is the primary process, can disrupt the KH structure (Faganello & Califano, 2017; Ma et al., 2014a, 2014b). The unprecedented high-resolution measurements provided by NASA's Magnetospheric Multiscale (MMS; Burch et al., 2016) mission, have enabled a more detailed study of the KH instability and its interplay with small-scale processes, like magnetic reconnection, thus allowing a better understanding of the different occurrence rates of the instability under southward and northward IMF. The first MMS observation of southward KH instability showed the presence of lower hybrid drift (LHD) waves at the trailing edges of the vortices, where the magnetic field lines are more compressed (Blasl et al., 2022). This process contributes to further mixing the plasma and can trigger magnetic reconnection at the electron scale (Nakamura et al., 2022; Blasl et al., 2023).

In this work, we compare two KH observations during northward and southward IMF orientations, respectively, on September 8, 2015 and September 23, 2017 (Eriksson et al., 2016; Blasl et al., 2022). Specifically, we focus on the kinetic features that characterize the KH structures at their boundaries and at their center. Previous studies have shown higher distortion of the ion velocity distribution functions (VDFs) at the center and stronger magnetic gradients at the boundaries both in in-situ observations and kinetic hybrid simulations (Settino et al., 2020, 2021). To identify such regions, in our analysis, we exploit the mixing parameter, a single-spacecraft quantity introduced in a previous paper by Settino et al. (2022). The mixing parameter takes into account the distinct particle energies in the magnetosphere (MSP) and magnetosheath (MSH), thus distinguishing where the particles are coming from. The outline of the paper is the following: in Section 2, we show an example vortex crossing for both the northward and southward IMF configurations; in Section 3, we analyze the properties at the boundaries and inside the crossings, pointing out the non-thermal features that arise; then, to give a better insight into such characteristics, in Section 4, we further analyze them in a minimum variance frame; finally, in Section 5, we discuss our results and state the conclusions.

2 Case study: KH events under northward and southward IMF

In this section, we compare two KH events observed by MMS during northward (NKH) and southward (SKH) IMF conditions at the Earth's magnetopause respectively on September 8, 2015 and on September 23, 2017 (see Eriksson et al., 2016; Blasl et al., 2022, for a detailed analysis of each event). During both KH events, MMS was located on the dusk side magnetopause but at different distances from the nose of the Earth's magnetopause. During the NKH event, the spacecraft observed KH fluctuations at about [5, 7, 0] R_E, before the terminator; while during the SKH event, they were observed farther in the flank, beyond the terminator at about [−10, 21, 6] R_E. We analyze data from MMS1 spacecraft. We use particle data from the Fast Plasma Investigation (FPI Pollock et al., 2016) with a cadence of 4.5 s in fast mode for both ions and electrons, magnetic field data from the FluxGate Magnetometer (FGM; Russell et al., 2016) with a resolution of 16 Hz in survey mode and spacecraft potential from the electric field double probe (EDP; Ergun et al., 2016; Lindqvist et al., 2016) with a resolution of 32 Hz in fast mode.

2.1 Overview of KH waves/vortices observation

We show an overview of the NKH event in panels (a)-(f) of Figure 1. During this event, MMS crossed the magnetopause boundary starting from the magnetospheric side, between 09:00 - 09:21 UTC, and exiting into the pure magnetosheath after 11:27 UTC. During its crossing, the spacecraft observed more than 1 hour of periodic or quasi-periodic fluctuations identified as surface waves or vortices excited by the KH instability (see Eriksson et al., 2016; W. Li et al., 2016, for further details). The encounters of the unperturbed magnetosphere (MSP) and magnetosheath (MSH) are also highlighted by the red and blue shades in Figure 1. Between these two regions, the spacecraft observed a long interval of quasi-periodic fluctuations (yellow shade) where the cold dense MSH plasma coexists with the hot tenuous magnetospheric one. These perturbations are clearly observed in several quantities, like, both the ions and electrons energy spectrograms, E_i, E_e (panels a and b), the ion density, N (panel c) and the ion and electron temperatures, T_i and T_e (panel d). In addition, MMS observed a preexisting boundary layer as indicated by the electron energy spectrogram in panel (b). Indeed, besides the high energy electron population of magnetospheric origin and the low energy MSH electrons, the spacecraft observed a third populations with energies in the range [200 1000] eV, intermediate between the MSP and MSH. This intermediate electron population has been associated to magnetic reconnection at mid-latitude, that would connect the MSH and MSP sides, thus allowing the heated MSH electrons from mid-latitude to reach the MMS location at lower latitudes (Vernisse et al., 2016; Eriksson et al., 2021). As a consequence of this pre-existing boundary layer, the density jump at the magnetopause is lowered, thus favoring the development of KH instability (Nakamura et al., 2017).

In panels (e) and (f) both the magnetic field and ion bulk velocity are shown in a local boundary coordinate system (lmn) as defined by Settino et al. (2022): The m-vector is along the wave vector of the KH perturbations, which is close to the bulk flow direction, the n-vector is chosen perpendicular to and directed outward in respect with the magnetopause boundary, and finally the l-vector completes the orthogonal system and is directed close to the north-south direction in the Geocentric Solar Ecliptic system (GSE). We highlight that to make the notation consistent with the SKH event and avoid any confusion, we have reversed the m-component along the anti-flow direction and consistently reevaluated the l direction. Therefore, the orthonormal versors written in the GSE system are: $l = [0.17,\ 0.11,\ 0.98]$, $m = [0.76,\ -0.64,\ -0.06]$, $n = [0.62,\ 0.76,\ -0.19]$. Panel 1e shows an almost constant B_l-component (blue line) with values close to the total magnetic field magnitude (black line), thus indicating a strongly northward IMF configuration. The other components, B_n and B_m, are close to zero but, during the KH interval, they display bipolar changes, corresponding to boundaries and narrow current sheets.

Finally, in panel (f), a clear shear flow is observed along the m-direction with a jump of about 400 km s^{-1} while period fluctuations around zero can be observed in the other two components, V_n, V_l.

Figure 1. Overview plots of two Kelvin-Helmholtz event observed by MMS1 during September 8, 2015 under Northward IMF orientation (top) and during September 23, 2017 under Southward IMF conditions (bottom). We show: (a), (g) ion energy spectrograms; (b), (h) electron energy spectrograms; (c), (i) particle density; (d), (j) ion and electron kinetic temperatures; (e), (k) three components of the magnetic field in a local boundary normal coordinate system LMN (see manuscript for a more detailed explanation) together with its magnitude; (f),(l) three components of the ion bulk velocity in a global coordinate system LMN. The magnetosperic and magnetosheath crossings are also highlighted by the red and blue shades, respectively.

The SKH event is very different from the NKH. The overview plot in panels (g)-(n) of Figure 1 shows that the spacecraft observed the boundary layer during the whole interval. Nonetheless, due to the outward motion of the magnetopause, it is possible to identify intervals with typical properties of the MSH and MSP regions. In particular, the ion and electron energy spectrograms (panels 1g and 1h) show the presence of low energy plasma between 15:56:20 - 15:58:00 UTC (blue shade) and high energy particles between 16:55:00 - 16:57:20 UTC (red shade). In correspondence of the blue shade, the density (panel 1i) is quite high (about 13 cm^{-3}); conversely, both ions and electrons temperatures (panel 1j) are very low (T_i = 150 eV and T_e = 30 eV). In addition, a high speed ion bulk flow (magnitude of about 300 km s^{-1}) is observed in panel 1l. All together these features are consistent with the crossing of a MSH-like plasma. On the other hand, in the red shade, an opposite behavior is observed, with respect to the blue one, for the density and temperatures. Indeed, a plasma characterized by a lower density (less than ~ 1 cm^{-3}) and higher ion and electron temperatures is observed. Moreover, the ion bulk velocity is close to zero, which is consistent with the crossing of a MSP-like plasma.

During this boundary layer crossing, MMS observed 1-hour fluctuations (yellow shade) consistent with KH waves/vortices (see Blasl et al., 2022, for further details). Contrary to the NKH fluctuations with a clear periodicity, the SKH event is characterized by more fragmented and less periodical structures. These feature seems to be typical for KH instability under southward IMF orientation (Hwang et al., 2012). 2D and 3D PIC simulations performed with a similar setup as the SKH event, have investigated this aspect of KH instability, suggesting that secondary instabilities like RT and LHD instabilities, can deform the KH waves/vortices and affect their periodicity (Nakamura, 2021). Moreover, for this event, signatures of such secondary instabilities were also observed by MMS (Blasl et al., 2022). We highlight that the vectors are displayed in a local boundary system defined as in Blasl et al. (2022) and consistent with the one discussed for the NKH event. Indeed, the m-vector is along the plasma anti-flow direction, n is perpendicular to the magnetopause boundary and directed outward and finally, l, which is close to the south-north direction, completes the orthonormal system. Therefore, in the SKH event, the new vectors written in GSE coordinates are: $l = [0.00,\ -0.29,\ 0.96]$, $m = [0.96,\ -0.28,\ 0.09]$, $n = [0.29,\ 0.91,\ 0.28]$. During the KH interval, between 15:30 - 16:30 UTC, the energy spectrograms show the co-existence of MSH-like and MSP-like particles and fluctuations in several plasma moments, namely density, ion and electron temperatures and ion bulk velocity, as well as in the magnetic fields. Specifically, sharp boundaries can be identified in the B_l-component (panel 1k) which is negative in the MSH-like intervals and positive in the MSP-like intervals, thus highlighting that the IMF is oriented southward.

2.2 Single vortex crossing

To statistically investigate the characteristics of KH waves/vortices and point out their differences and similarities under different IMF orientations, we use a mixing parameter, μ, introduced by Settino et al. (2022). This quantity is defined independently for ions (μ_i) and electrons (μ_e), based on their energies in the MSH-like and MSP-like regions. Since these two regions have distinct energies at the Earth magnetopause, μ allows us to identify where the particles are coming from. Hereafter, we briefly show the definition and main properties of such quantity and refer to Settino et al. (2022) for a more detailed discussion. The mixing parameter is a normalized quantity which ranges between $[-1,\ 1]$ and is defined as follows:

$$\mu_\alpha = \frac{\bar{\sigma}_{\alpha,a} - \bar{\sigma}_{\alpha,b}}{\bar{\sigma}_{\alpha,a} + \bar{\sigma}_{\alpha,b}}, \tag{1}$$

$$\sigma_{\alpha,a(b)} = \int_{E_{\alpha,a(b)}} f_\alpha(E,t)\ dE, \tag{2}$$

where $\sigma_{\alpha,a(b)}$ is the omni-directional particle distribution function, $\alpha = i, e$ is the index running on the particle species, a is the energy range corresponding to a MSH-like (low energy) particles, b is the energy range corresponding to MSP-like (high energy) particles, and finally the overline $(\overline{...})$ indicates that the quantity has been normalized to its maximum value. Because of this definition, the extreme values, -1 and 1, correspond to the non-mixed plasma of the pure MSP and MSH, respectively, while 0 corresponds to the highest degree of mixing. Moreover, the intervals [-1,0) and (0,1] correspond, respectively, to a plasma dominated by particles of magnetospheric or magnetosheath origin. In addition, as already shown in Settino et al. (2022), the range -0.5 and 0.5 identify the region with higher mixing.

The mixing parameter has already been applied to the NKH event to identify the spacecraft trajectory across the KH structures and their evolutionary stage (Settino et al., 2022). In this case each KH wave/vortex has been analyzed into the mixing-parameter space generated by both μ_i and μ_e. Based on the trajectory of the particles in this space, three different types of crossings were identified: i) waves (straight line trajectory), ii) steepened waves (simple loop trajectory) and iii) rolled-up vortices (complex loop trajectory with multiple twists). Such a classification showed the second type of crossings (i.e. steepened waves) to be the predominant one. Conversely, in the present study, we focus on two specific regions of the KH waves/vortices, namely boundaries and center, and investigate their main properties. In the following, we show that the electron mixing parameter, μ_e, is a good candidate to identify the center and the boundaries of KH waves/vortices. For this purpose, in Figure 2, we only show a single vortex crossing for the NKH (left) and SKH (right) event. The wave/vortex region is highlighted by the vertical red solid lines, while the two boundaries (B) and the center (C) are divided by the vertical red dashed lines.

At first, we focus on the NKH event. In Figure 1a-e, we choose one of the steepened wave crossings which are more representative of this event. Panel 1a shows an almost constant B_l-component (blue line) with values close to the total magnetic field magnitude (black line), thus indicating a strongly northward IMF configuration. Between 10:26:27.97 UT and 10:26:32.00 UT, the spacecraft observe a smooth transition in both the magnetic field (panel a) and ion bulk velocity (panel b) components; thus suggesting that MMS is crossing a smooth boundary of the KH structure. Such boundary can be clearly observed in the electron energy spectrogram (panel 1c). Indeed, close to the first vertical red dashed line, we observe a transition from a plasma dominated by low energy electrons to a plasma where the intermediate electron energy population starts to dominate. On the other hand, the ion energy spectrogram (panel 1d) doesn't change. This region is consistent with the crossing of the first KH wave/vortex boundary.

Figure 2. Plot of a single KH crossing during the September 8, 2015 event under a Northward IMF (left) and during the September 23, 2017 event under a Southward IMF (right). From top to bottom we show: (a), (e) three components of the magnetic field in a global coordinate system LMN (see text for a more detailed explanation) together with its magnitude; (b), (f) electron energy spectrogram; (c), (g) ion energy spectrogram; (d), (h) ion (black) and electron (red) mixing parameters. The energy ranges used to evaluate the mixing parameters are shown on top of the energy spectrograms. Boundary regions (B) are identified by the interval between the red vertical solid and dashed lines, while the center (C) is highlighted by two red vertical dashed lines. The black horizontal solid line indicate the threshold value of the electron mixing that distinguishes between boundaries and center. Finally, the yellow shade in panel (e), indicate the time of the 3D ion velocity distribution function displayed in Figure 7.

After this boundary, the spacecraft enter a region characterized by a change in the sign of B_m and B_n and a consistent decrease in the shear velocity (V_m) which assumes values intermediate with respect to the MSP (almost quiet plasma) and the MSH (~ 300 km s^{-1}). Such features are consistent with the KH dynamics during which, due to the velocity shear, a centrifugal force develops and produces a twist of the magnetic field lines. To balance such a force, a pressure gradient is generated that tends to confine the low density MSP plasma at the center. In addition, both the ion and electron energy spectrograms show the co-existence of high and low energy particles, with the former being increasingly dominant. Therefore, this region is consistent with the crossing of the inner part of KH wave/vortex (i.e. center). Finally, in correspondence of the second vertical dashed line, the low energy MSH plasma becomes again the dominant one and clear boundaries are observed in both the electron and ion energy spectrograms. Moreover, the shear velocity magnitude, $|V_m|$ start to increase again and similar properties as in the first boundary region are observed for both plasma quantities and fields. The spacecraft is then crossing the second KH wave/vortex boundary.

It is worth pointing out that the boundaries observed in the plasma and fields quantities are also well identified by the electron mixing parameter. In panel 1e we show the ion (black curve) and electron (red curve) mixing parameters, which have been defined by using the energy ranges shown in Figure 1c, 1d. Specifically, μ_i, is defined by using the low energy range $E_{i,L} = [20,\ 3000]$ eV and the high energy range $E_{i,H} = [3,\ 20]$ keV. On the other hand, for the electron mixing, μ_e, we use the intermediate energy range $E_{e,M} = [200,\ 700]$ eV and the low energy range $E_{e,L} = [20,\ 60]$ eV. It is immediately evident that the crossing from the KH boundary to the center and vice-versa, corresponding to the inner boundaries (red vertical dashed lines at $t_{in}^{(1)}$, $t_{in}^{(2)}$), is well identified by the threshold $\mu_e = 0.5$. The outer boundaries (red vertical solid lines at $t_{out}^{(1)}$, $t_{out}^{(2)}$), instead, are identified by using both the electron mixing parameter, plasma quantities and magnetic field. Specifically, we consider regions where $\mu_e \geq 0.5$ and magnetic field, ion bulk velocity, density and temperature have quite constant values but lower than the ones observed in the unperturbed MSH. This would also correspond to exclude values of μ_e which are close to 1, as by definition they indicate the crossing of unperturbed MSH plasma that the spacecraft can observe between two consecutive KH structures. It is worth mentioning that μ_i and μ_e, in general, can have a different behavior as clearly shown in panel 1e where the electron mixing is consistently lower than the ion mixing at the beginning of the interval, while has a similar profile close to the second boundary region. However, for the structures that we are considering (KH waves/vortices have dimensions of several ion inertial lengths) the electrons are magnetized and therefore respond faster to changes in the magnetic field topology; thus μ_e represents a better candidate than ions for the identification of the boundaries and center of the KH structures.

Here, we consider the SKH event. The southward IMF orientation is clearly identified by the negative B_l component (panel 1f) in the MSH, outside the two boundary regions (red vertical lines). The first boundary region is encountered between 15:40:31.22 UT and 15:40:54.94 UT. In this interval the magnetic field magnitude (black curve in panel 1f) locally increases, the B_l-component has a quite sharp transition from negative to positive values and the B_n and B_m components have different signs. The same features are also observed in the second boundary region between 15:42:32.00 UT and 15:43:01.25 UT, thus highlighting that the boundaries are quite symmetric. Such symmetry in the boundaries can be observed also in other quantities like the electron (panel 1h) and ion (panel 1i) energy spectrograms and both ion and electron mixing parameter (panel 1l). The center of the crossing shows a positive and quite steady B_l-component (panel 1f), a decreasing shear velocity V_m (panel 1g) and a high energy particle population of MSP origin in both spectrograms (panels 1h, 1i). We also point out that the ion energy spectrogram shows, in the center but very close to the inner boundaries, a more MSH-like plasma due to the excitation of lower hybrid drift (LHD) waves that contribute to plasma diffusion at the boundaries and generate an extra mixing inside the structures (Blasl et al., 2022). Such feature can be also recognized in the ion mixing parameter, especially close to the first boundary region where μ_i remains lower than μ_e suggesting that it enters more smoothly the high energy region. The mixing parameters also highlight some other interesting differences between these two crossings. For instance, during the NKH event, μ_e is lower than μ_i not only at the boundaries but also during the first part of the crossing, while, during the SKH event, the two mixing parameters follow each other quite well except for some discrepancies at the boundaries where conversely μ_i is lower than μ_e. We anticipate that such a feature is not limited to these two crossings but is typical for all the structures observed during these events as observed in the statistics discussed in the next Section.

3 Kinetic properties of KH crossings

In this section, we statistically study the properties at the boundaries and center of all the KH crossings for both events and point out differences and similarities between the NKH and SKH observations. The boundaries and center of each crossing have been identified by using the electron mixing parameter as discussed in the previous Section and shown in Figure 1 for two specific crossings. Therefore, we have identified the inner boundaries as the time at which $\mu_e = 0.5$ and fixed the two outer boundaries starting from these times. Each crossing of the NKH or SKH event have in general different duration of the boundary regions, as can be easily observed in Figure 2. To take into account this and make a one-to-one comparison among all the KH crossings of the same event, we have normalized each crossing to the duration of the inner boundaries crossing, i.e. $\hat{t} = (t - t_{in}^{(1)})/(t_{in}^{(2)} - t_{in}^{(1)})$. Therefore, $\hat{t} = 0$ corresponds to the first inner boundary ($t_{in}^{(1)}$in Figure 2), while $\hat{t} = 1$ corresponds to the second inner boundary ($t_{in}^{(2)}$ in Figure 2). Thus, the center of the KH waves/vortices is identified by the time interval $0 < \hat{t} < 1$, while the two boundary regions are $\hat{t} \leq 0$ and $\hat{t} \geq 1$.

We point out that, contrary to the center of the KH waves/vortices, KH boundaries have a shorter extension which could be not well resolved by using fast measurements. Therefore, we have evaluated the average duration of the boundary region and found that it is ~ 18.5 s for the SKH event and about 8.6 s for the NKH event. While the boundary region is well resolved for the SKH event and only 8.3% of the boundaries have a resolution lower than MMS, the conditions worsen a bit for the NKH event. Indeed, in this case the extension of the boundaries is closer to the MMS resolution and more boundaries, about 37.3%, are not well resolved by the spacecraft. However, during the NKH event much more KH crossings (about 69) are observed, thus consistently increasing the statistics for the boundaries. Considering the high number of KH crossings for the NKH event and the long extension of the boundaries for the SKH and since we are interested in the general properties of the boundaries which are well above the ion scale, fast mode data can provide a good statistic.

Figure 3. Histograms of the ion and electron mixing for the whole KH vortex crossings during the Northward (left columns) and Southward (right column) IMF. The time interval of each vortex crossing has been normalized as described in the text, i.e. $(t - t_{in}^{(1)})/(t_{in}^{(2)} - t_{in}^{(1)})$, so that for each crossing 0 and 1 correspond to the times of the two inner boundary crossings. The vertical red dashed lines separate the boundary regions from the center according to the mixing parameters values. From top to bottom the panels show: (a), (d) the ion mixing; (b), (e) the electron mixing; (c), (f) the difference between ion and electron mixing.

In Figure 3, we show the mixing degree of electrons and ions for all the structures during NKH and SKH events. Keeping in mind that the mixed region corresponds to the range $\mu_e \in [-0.5, 0.5]$ (blue shade), in panel (a) we observe that ions are predominantly mixed at the center of the structures. A different behavior is observed instead for μ_e that is mixed close to the boundaries (see panel 2b). Moreover, while μ_i displays an asymmetric shape with a smoother transition close to the first boundary and a sharper one close to the second boundary crossing, a symmetric profile is observed for the electron mixing as also highlighted by panel (e) in Figure 1. On the contrary during the SKH event, we clearly observe an ion population of MSP origin ($\mu_i \simeq -1$) at the center and a quite symmetric shape with sharp transition at both boundaries. In this case, mixed particles are well confined in the regions close to the boundaries. The same shape is observed for the electron mixing parameter in panel 2e, thus suggesting a similar ion and electron dynamics.

The different characteristics of the KH structures during each event can be attributed to two factors: i) the development of more rolled-up vortices during the NKH event; ii) the location of the spacecraft relative to the magnetopause boundary. Indeed, the high mixing observed at the center of the structures would suggest that KH vortices are more rolled-up during the NKH than SKH event. As a further confirmation, we have also checked the behavior of the ion and electron mixing parameters (not shown) during the last part of the NKH interval, when an increasing number of rolled-up vortices is observed (Settino et al., 2022). We found that the counts tend to be confined inside or close to the blue shade, thus suggesting that rolled-up structures are mainly responsible for the plasma mixing enhancement. In addition, the crossing of pure MSP particles inside the SKH crossings is not only connected to the early stage of the KH structures but it is also consequence of the fact that the magnetopause boundary is moving outward, thus MMS encounters more and more magnetospheric particles. Indeed, Blasl et al. (2022) highlighted that short interval of almost pure MSH plasma are observed only at the very beginning of the SKH event, while at later times, MSH-like encounters show low density values compatibles with a more boundary layer plasma.

In order to better quantify such differences between the ion and electron mixing parameters, in panels 2c and 2f we show the quantity: $\Delta\mu = |\mu_i| - |\mu_e|$. This definition takes into account the fact that the highest degree of mixing is associated to the values closest to zero, so when $|\mu_i| > |\mu_e|$ it means that electrons are more mixed than ions and vice-versa when $|\mu_i| < |\mu_e|$. It is worth noticing that the largest (or lowest) is this difference, the more the two mixing parameters follow a different behavior. Conversely, when $|\mu_i| - |\mu_e| = 0$ the two mixing parameters perfectly follow each others. Then, by using $\Delta\mu$, we can easily observe that during the NKH event, electrons experience higher mixed close to the boundaries, while ions are more mixed at the center of the KH waves/vortices. A very different behavior is observed during the SKH event for μ_i and μ_e. Indeed, ion and electron mixing parameters follow each other very well at the center of the KH structures, while more mixed ions are observed at the boundaries. It is worth pointing out that a higher electron than ion mixing is also observed inside the vortices close to the inner boundaries, specifically $[0, 0.2]$ and $[0.85, 1]$. The development of LHD waves at the boundaries of KH waves/vortices, due to strong magnetic field compression, could account for the diffusion of electrons and the enhanced mixing highlighted by $\Delta\mu$.

Figure 4. Histograms of the ion (a), (c) and electron (b), (d) temperature anisotropy for the Northward (left columns) and Southward (right columns) IMF. The horizontal black dot-dashed lines indicate the isotropic temperature.

To further characterize the properties of KH waves/vortices, in Figure 4, we also investigate ions and electrons temperature anisotropies. As the KH instability leads to the mixing of MSH and MSP plasma, also ions and electrons temperatures are expected to assume values intermediate in respect with the two sides of the shear layer. It is immediately evident that the strongest anisotropy is observed in the NKH event, during which the ion temperature anisotropy reaches a value of ~ 3 at the boundaries. At the center, although $T_{i,\perp}/T_{i,||}$ is statistically close to isotropic, we observe both parallel and perpendicular temperature anisotropies. It is worth pointing out that the ion anisotropy displays the same asymmetry as the ion mixing due to the presence of a few counts with higher perpendicular temperature either close to the leading edge and at the center connected to rolled-up vortices. This is in agreement with recent studies that observed an enhancement of rolled-up vortices due to changes in the conditions at the bow-shock towards the end of the KH interval (Settino et al., 2022). Conversely, electrons are close to isotropic at the boundaries, while at the center a strictly parallel anisotropy is observed. This is not surprising as electrons quickly respond to changes in the magnetic field topology.

Interestingly enough, during the SKH event, both ions and electrons are isotropic at the boundaries while at the center they have a different behavior. Ions have a higher perpendicular temperature anisotropy, while electrons are very close to isotropic but with either small parallel and perpendicular temperature anisotropies. Such observations are in agreement with both simulations and *in situ* observations showing the presence of a change in the ion temperature anisotropy direction in correspondence of the KH boundaries (Settino et al., 2020, 2021). It is worth pointing out that, while isotropic ion temperature at the boundaries seems to be a common feature to all KH vortices, at the center, instead, the ion temperature anisotropy doesn't have a unique trend. Both upstream solar wind conditions and development of secondary instabilities could affect its behavior, as well as the evolutionary stage of the KH structure itself.

3.1 Statistical analysis over the whole KH interval

The analysis shown in the previous sections, based on the identification of the inner and outer boundaries, is rather difficult due to the fact that each KH crossing has to be carefully checked by eye to properly identify the outer boundaries. Therefore, such approach is less suitable for a statistical study which would include many KH observations under different solar wind conditions and a train of crossings for each event. In this section, we show that the electron mixing parameter can enable a more straightforward analysis of the kinetic properties at the boundaries and center of the structures providing the same results as the identification of the single crossings.

In panels 5a and 5b, we show again the ion, $T_{i,\perp}/T_{i,||}$, and electron, $T_{e,\perp}/T_{e,||}$, temperature anisotropies. Contrary to Figure 4, here we plot the whole KH interval in function of the electron mixing parameter. As widely discussed, values of $\mu_e \geq 0.5$ (yellow shade in Figure 5) corresponds to the boundary regions of the KH waves/vortices, while $\mu_e < 0.5$ (blue shade) corresponds to the inner region of the KH structures. We point out that in this case we exclude not only the values close to 1 but also to -1 to take into account both the pure MSH and MSP regions that the spacecraft could observe between one crossing and the other, without affecting the outcome of the analysis. By using this approach, the first and second boundary of the KH structures can't be separated but are both included in the boundary region. We clearly observe that the same statistical properties are recovered at the boundaries and center of the KH waves/vortices when comparing Figure 4 with panels 5a and 5d. For example, if we focus on the NKH event, the same strong perpendicular ion temperature anisotropy is recovered at the boundaries, while at the center the ions are close to isotropic with a predominance of perpendicular anisotropy. Furthermore, isotropic electrons at the boundaries and strictly parallel at the center are also recovered.

Figure 5. Scatter plot of non-thermal features of KH vortices as a function of the electron mixing parameter. In the panels we show: (a) ion temperature anisotropy; (b) ion agyrotropy; (c) ion non-Maxwellianity; (d) electron anisotropy; (e) electron agyrotropy; (f) electron non-Maxwellianity for the northward (green bullets) and southward (red bullets) IMF orientation. The blue and yellow shades in each panel indicate the two different regions identified by the electron mixing parameter (i.e. center and boundaries, respectively).

Since the electrons move faster along the magnetic field lines and quickly respond to changes in the magnetic field, μ_e represents a good candidate for the identification of the boundaries of KH structures as discussed already in Section 2. This is particularly evident in panels (d) and (j) of Figure 2, where μ_e follows very well the bipolar changes in the magnetic field as well as the reversal in the SKH event at the boundaries, and the decrease of the ion bulk velocity at the center. Moreover, as it takes into account the particles origin, μ_e automatically separates the different plasma populations based on where they are coming from. Thus, as a next step, we consider the whole KH interval for both events, which correspond to the time interval [10:09:00, 11:30:00] UT for the NKH observation and [15:30:00, 16:30:00] UT for the SKH event (yellow shades in Figure 1). As the electron mixing parameter well reproduces the results obtained from the single crossings analysis, we take advantage of this quantity to investigate in more details some kinetic features associated with KH structures, with a particular focus on agyrotropy and local non-thermal features quantified via the non-Maxwellianity measure. The ion, Q_i and electron, Q_e, agyrotropy are evaluated by using the components of the pressure tensor, $\mathbf{P}_{i(e)}$, rotated in the reference frame in which one of the axes is along the local magnetic field and the two perpendicular pressures are equal (Swisdak, 2016):

$$\mathbf{P}_{i(e)} = \begin{pmatrix} P_{||} & P_{xy} & P_{xz} \\ P_{xy} & P_{\perp} & P_{yz} \\ P_{xz} & P_{yz} & P_{\perp} \end{pmatrix} \quad (3)$$

$$Q_{i(e)} = \frac{P_{xy}^2 + P_{xz}^2 + P_{yz}^2}{P_{\perp}^2 + 2P_{\perp}P_{||}}; \quad (4)$$

where $\mathbf{P}_{i(e)}$ is by property symmetric, and the subscripts, indicating the particle species, have been dropped in the components of the pressure tensor for an easier reading. $Q_{i(e)}$ ranges from 0 (fully gyrotropic configuration) to 1 (maximum agyrotropy, where all non-diagonal elements of the pressure tensor contribute to the agyrotropy). We observe a similar behavior for Q_i and Q_e in panels 5b, 5e. During both the NKH and SKH events the agyrotropy parameters reach higher values at the center and close to the boundaries of the KH waves/vortices. However, $Q_{i(e)}$ are very small in all cases ($\sim 0.2\%$ for electrons

Table 1. NKH event. Maximum values of non-local thermal features of KH structures

Region	ϵ_i	ϵ_e	$T_{i,\perp}/T_{i,\|\|}$	$T_{e,\perp}/T_{e,\|\|}$	$Q_i \times 10^{-2}$	$Q_e \times 10^{-3}$
MSP	0.41	0.09	3.03	1.06	0.20	0.1
MSH	0.38	0.11	1.60	0.83	0.75	0.2
Center	0.67	0.13	3.15	0.99	1.19	1.6
Boundaries	0.50	0.13	3.08	1.01	1.39	0.9

Table 2. SKH event. Maximum values of non-local thermal features of KH structures

Region	ϵ_i	ϵ_e	$T_{i,\perp}/T_{i,\|\|}$	$T_{e,\perp}/T_{e,\|\|}$	$Q_i \times 10^{-2}$	$Q_e \times 10^{-3}$
MSP	4.47	1.12	1.25	1.06	2.57	0.3
MSH	3.81	0.35	1.68	1.25	0.43	0.4
Center	2.95	0.71	1.72	1.05	1.95	1.4
Boundaries	3.78	0.41	1.43	1.08	0.74	0.5

and about 10 times more for ions), thus suggesting that the particle VDFs remain close to gyrotropic. The maximum values reached by the ion and electron agyrotropies in each region (i.e. boundaries, center, MSP and MSH) is clearly shown in Table 1 for the NKH event and 2 for the SKH event.

As KH vortices evolve, an energy cascade towards small scales is generated due to the nonlinear coupling of the modes. This mechanism can lead to complicated non-Maxwellian deformations. Deviations from the Maxwellian shape have been quantified via the non-Maxwellianity measure, defined for both ions and electrons and for a fixed time as in Greco et al. (2012)

$$\epsilon_{i,(e)} = \frac{1}{n_{i,(e)}} \sqrt{\int_{\mathrm{v},\theta,\phi} \left[f_{i,(e)}(\mathrm{v},\theta,\phi) - g_{i,(e)}(\mathrm{v},\theta,\phi)\right]^2 \mathrm{v}^2 \sin\theta \, \mathrm{dv d}\theta \mathrm{d}\phi} \tag{5}$$

where, $n_{i,(e)}$ is the particle density, $f_{i,(e)}$ is the observed distribution function and $g_{i,(e)}$ is the associated Maxwellian built with the moments of $f_{i,(e)}$. In order to have a dimensionless quantity, we also multiplied by $v_A^{3/2}$ (v_A being the Alfvén speed in the magnetosheath). Consequently, $\epsilon_{i,(e)} = 0$ corresponds to a Maxwellian distribution. Both ion and electron non-Maxwellianity can be artificially increased by the noise associated to low counts statistics (Graham et al., 2021). Moreover, the electron non-Maxwellianity can be affected by photoelectrons, which can contaminate the low energy channels. During both the NKH and SKH event, the Active Spacecraft Potential Control (ASPOC; Torkar et al., 2016) was active, indeed the spacecraft potential was less or very close to $+4V$ (its maximum value is 3.6 V for NKH and 4.7 V for SKH event), thus not affecting MMS measurements. However, photoelectrons generated inside the detector as well as ion plumes emitted from the spacecraft when ASPOC is active can still affect the electron VDFs at low energies (Gershman et al., 2017; Barrie et al., 2019). Therefore, to reduce these artificial and instrumental noises, we have integrated ϵ_e in the energy range [20 eV, 21 keV] for the NKH event and [15 eV, 21 keV] for the SKH event.

The effect of low count statistics would be stronger at the center of the KH waves/vortices, where the low density plasma tends to be confined due to the vortical motion. Thus, we have estimated both ϵ_i and ϵ_e by averaging the VDFs on different times and verified that the results do not significantly change. For completeness, we also checked local non-thermal features by using another recently defined non-Maxwellianity measure (Graham et al., 2021):

$$\tilde{\epsilon}_{i,(e)} = \frac{1}{2n_{i,(e)}} \int_{\mathrm{v},\theta,\phi} \left| f_{i,(e)}(\mathrm{v},\theta,\phi) - g_{i,(e)}(\mathrm{v},\theta,\phi) \right| \mathrm{v}^2 \sin\theta \; \mathrm{dv d}\theta \mathrm{d}\phi \tag{6}$$

We observe that there is a good correlation between the two methods when electrons are considered, but not for ions (see Figure S1 in supplementary material). Indeed, the latter suggests that $\tilde{\epsilon_i}$ reaches its highest value in the MSH, while both center and boundaries have non-Maxwellianity values ranging between the ones in the MSP and MSH side. However, the ion VDFs are clearly distorted and show field-aligned beams both at the center and at the boundaries (Eriksson et al., 2021). Therefore, in panels 5e and 5f we decided to show only $\epsilon_{i,e}$ that we find more representative in this case. The largest non-thermal features are observed during the NKH event. Indeed, in the vortex region, both ions and electrons non-Maxwellianities reach higher values in the vortex region (center or boundary) than in the MSP or MSH (see also Table 1); thus suggesting that processes other than particle diffusion are triggered. On the other hand, during the SKH event, both ion and electron VDFs are less distorted and show values intermediate to the MSH and MSP (see Table 2). Such strong distortions during the NKH event are analyzed in more details in the next section.

4 Kinetic features in a Minimum Variance Frame

We observed that, for the NKH event, non-local thermal features are higher at the center or boundary regions than in the unperturbed MSP and MSH sides (Figure 5 and Table 1). On the contrary, during the SKH event, these same quantities reach intermediate values with respect to the MSH and MSP sides. Therefore, to get an insight into such enhancement, we focus now on the NKH observations and study in more details the ion and electron VDFs in a minimum variance frame (MVF) defined by the temperature tensor (Servidio et al., 2012)

$$\mathbf{T}_{i(e)} = \frac{m_{i(e)}}{n_{i(e)}} \int_{\mathrm{v},\theta,\phi} (\mathbf{v} - \mathbf{V}_{i(e)})(\mathbf{v} - \mathbf{V}_{i(e)}) f_{i(e)}(\mathrm{v},\theta,\phi) \mathrm{v}^2 \sin\theta \; \mathrm{dv d}\theta \mathrm{d}\phi \; , \tag{7}$$

where,$m_{i(e)}$ is the particle mass, $n_{i(e)}$ is the particle density, $\mathbf{V}_{i(e)}$ is the particle bulk velocity and $f_{i(e)}(\mathrm{v},\theta,\phi)$ is the distribution function observed by MMS. At each time we evaluate the eigenvalues, $\{\lambda_1, \lambda_2, \lambda_3\}$ (that we ordered according to the convention as: $\lambda_1 > \lambda_2 > \lambda_3$) and the associated normalized eigenvectors, $\{\hat{\mathbf{e}}_1, \hat{\mathbf{e}}_2, \hat{\mathbf{e}}_3\}$, for both species. We note that λ_j (with $j = 1, 2, 3$) are proportional to the temperature, while $\hat{\mathbf{e}}_j$ are the anisotropy directions of the VDFs. We point out that a Maxwellian distribution function does not have any preferential direction, indeed the tensor has a diagonal form and is degenerate ($\lambda_j = 1$). Conversely to the non-Maxwellianity parameter, $\epsilon_{i,(e)}$, that provides a more qualitative indication about the distortions in the particles VDFs, the analysis of the eigenvalues provides a more quantitative insight into the properties of symmetry of the distribution functions. In analogy to the approach used by Valentini et al. (2016), we compute the probability density function (PDF) conditioned to the values of the ion and electron non-Maxwellianity.

Figure 6. ion (top) and electron (bottom) PDFs conditioned to the values of the non-Maxwellianity parameters.

In Figure 6 we show the PDF of the ratios λ_1/λ_2, λ_1/λ_3, λ_2/λ_3 for two different ranges of values of the non-Maxwellianity: $0 \leq \epsilon_{i(e)} < \sigma_{i(e)}$ (black curve) and $\epsilon_{i(e)} \geq \sigma_{i(e)}$ (red curve), where $\sigma_{i(e)}$ is the standard deviation of $\epsilon_{i(e)}$. In Panel 6(a), the ion PDF peaks at $\lambda_1/\lambda_2 = 1$ when small values of ϵ_i are considered, while for larger values of

ϵ_i, the peak start to move to the right, the ion PDF becomes wider and higher tails start to appear. This suggests that the ion VDFs are more and more distorted, in agreement with kinetic hybrid simulation of turbulence (Valentini et al., 2016). On the other hand, in panels 6(b) and (c), the ion PDF peaks, resspectively, at $\lambda_1/\lambda_3 = 1$ and $\lambda_2/\lambda_3 = 1$ for both ranges of the ion non-Maxwellianity. Nonetheless, for $\epsilon_i > \sigma_i$, the ion PDF is wider. We point out that the local peak in the tail of the ion PDF at $\lambda_1/\lambda_3 \sim 3$ in panel 6b and at $\lambda_2/\lambda_3 \sim 2.6$ in panel 6c, corresponds to the MSH ions which have a strong perpendicular temperature anisotropy. Interestingly, panels 6(d) and (e) show a larger anisotropy when $\epsilon_e < \sigma_e$, whereas isotropic electrons are observed for the high range of electron non-Maxwellianity. Finally, we notice the Maxwellian behavior of electrons in panel 6(f) where a strong and collimated peak at $\lambda_2/\lambda_3 = 1$ is observed for any value of ϵ_e.

An enhancement in the non-Maxwellianity is typically connected to strong deformations of the particle VDFs whose main axis can consistently depart from the local magnetic field direction due to nonlinear effects (Servidio et al., 2012; Perrone et al., 2013; Settino et al., 2020). As KH instability is a multiscale phenomenon, it is of particular interest to investigate the alignment of the magnetic field with the principal axis of the VDF. Thus, we statistically analyzed the angle, θ, between the local magnetic field direction, $\mathbf{B}$, and the principal eigenvector, $\hat{\mathbf{e}}_1$, for both ions and electrons. The PDFs of these quantities are showed in Figure 7. Electrons display two peaks in correspondence of $\cos\theta = -1$ and $\cos\theta = 1$ (black curve), thus suggesting that the preferential direction for the electron VDFs is well aligned with the local magnetic field. The observation of two peaks in the parallel and anti-parallel directions could be associated to the double mid-latitude reconnection suggested for this event by both simulations and observations (Ma et al., 2021; Vernisse et al., 2016; Eriksson et al., 2021).

Figure 7. Left: PDF of the cosine angle between the local magnetic field direction and $\hat{\mathbf{e}}_1$ for electrons (black), ions (red), ion core (green) and ion tail (blue). The horizontal dashed line at 0.5 corresponds to the uncorrelated vectors. Right: 3D ion VDF in the MVF generated by the eigenvectors associated to the ion temperature tensor $\mathbf{T}_{i,tail}(\hat{\mathbf{e}}_{1,tail}, \hat{\mathbf{e}}_{2,tail}, \hat{\mathbf{e}}_{3,tail})$. 2D cuts in the planes generated by $(\hat{\mathbf{e}}_{1,tail}, \hat{\mathbf{e}}_{3,tail})$ and $(\hat{\mathbf{e}}_{2,tail}, \hat{\mathbf{e}}_{3,tail})$ are also showed. Moreover, the other two preferential directions $\hat{\mathbf{e}}_{1,tot}$ and $\hat{\mathbf{e}}_{1,core}$ as well as the local magnetic field direction $\mathbf{B}$ have been indicated.

An opposite behavior is observed for ions, whose PDF (green curve) peaks at $\cos\theta = 0$, suggesting that the main deformation of the ion VDFs are perpendicular to the local magnetic field direction. However, such behavior is in contrast with the field-aligned beam or double beams observed at the leading edges of several KH vortices (see Eriksson et al., 2021, for a detailed analysis of the ion VDFs). We note that the core of all the ion VDFs is strongly anisotropic with an elongation in the perpendicular direction to the local magnetic field. Since this is the main part of the distribution and has a higher weight than the tails, it tends to cover the effects of the beams. Thus, we separate the ion temperature tensor into the core, $\mathbf{T}_{i,core}$, and the tail part, $\mathbf{T}_{i,tail}$, and evaluate the associated eigenvectors $\hat{\mathbf{e}}_{j,core}$ and $\hat{\mathbf{e}}_{j,tail}$. In order to identify the core distribution, we consider the omnidirectional ion VDFs and evaluate the Maxwellian distribution that better fits the core of all the measured ion VDFs (see Figure S2 in supplementary material). We point out that this is a rather qualitative method but is sufficient for the purpose of this analysis. Once we determine temperature associated to the fitting Maxwellian distribution ($\mathbf{T}_{i,core}$), we evaluate the tail temperature tensor as $\mathbf{T}_{i,tail} = \mathbf{T}_{i,tot} - \mathbf{T}_{i,core}$.

Figure 7 clearly shows that when we remove the effect of the core, two peaks arise in correspondence of the parallel or anti-parallel directions to the local magnetic field (blue curve). Finally, we show an example of an ion VDF (right panel in Figure 7) in the MVF generated by the tail part of the stress tensor $\hat{\mathbf{e}}_{i,tail}$. The local magnetic field direction as well as the main eigenvector associated to the core and the full tensor are also displayed. The perpendicular anisotropy of the core is immediately evident and so is the field-aligned beam which accounts for the strong deviation from local thermodynamic equilibrium as shown by ϵ_i inside the KH structures.

5 Discussion and Conclusion

We present the application of a new quantitative measure, the plasma mixing parameter introduced in Settino et al. (2022) for electrons and ions, and demonstrate how it can help characterize and classify, in conjunction with non-thermal equilibrium considerations, the small-scale properties of KH waves/vortices and their evolution in the vicinity of the Earth's magnetopause. We investigated and compared two cases of KH structures generated under two different solar wind conditions at the magnetopause by using MMS in-situ measurements. In particular, we used as benchmarks the event of September 8, 2015 under northward IMF conditions and the event of September 23, 2017 under southward IMF orientation. Numerical simulations and spacecraft observations have highlighted typical signatures of magnetic reconnection at remote sites (mid- or high-latitudes) for the northward case (Vernisse et al., 2016; Ma et al., 2021; Eriksson et al., 2021). Such process of double mid-latitude reconnection is responsible for the electron population with intermediate energy and density between the magnetosphere and magnetosheath as discussed in Section 2. On the other hand, kinetic simulation performed under the same conditions as the southward KH event, showed the development of secondary instabilities, namely RT instability, that tends to elongate the vortices thus preventing their rolling and lower hybrid activity that tends to diffuse electrons close to the boundaries (Nakamura et al., 2022; Blasl et al., 2022).

To better characterize the mixing properties of the structures and the differences between the two KH events, we defined and used the ion and electron mixing parameters, a single-spacecraft quantity which take into account where the particles are coming from based on their energies (Settino et al., 2022). Since electrons quickly respond to the magnetic field changes, the electron mixing parameter can also very well distinguish the boundaries and center of KH structures. Both numerical simulations and in-situ measurements have highlighted that the KH instability development and evolution is affected by both remote and large-scale properties, like IMF configuration, as well as local mechanisms that are triggered by or competing with KH evolution (see for example Faganello & Califano, 2017, and references therein). Therefore, we suggest that the mixing parameters together with kinetic properties of the KH structures, like temperature anisotropies and non-Maxwellianity, can be connected and provide an insight into both local and remote processes affecting the instability.

In our analysis we observed that, during the northward event, electrons are more mixed at the boundaries, while ions are more mixed at the center. Interestingly, the southward KH event, instead, is characterized by low ion and electron mixing inside the structures. Indeed, mixed plasma is observed predominantly close to the boundaries, while at the center particles of magnetospheric origin dominate. Such behavior suggests that the northward event is characterized by more evolved KH vortices than the southward event, although, in the former, MMS was located close to the nose, and during the latter, in the flank magnetopause where more rolled-up vortices are expected (Lin et al., 2014). The symmetric shape observed for both ion and electron mixing may suggest the crossing of surface waves. However, the extended ion and electron mixing close to inner and outer boundaries suggest instead that KH vortices are in a more advanced phase. Numerical simulations performed under conditions similar to those of the southward event showed the development of the RT instability triggered by the strong density jump at the boundary (Nakamura et al., 2022). Such instability tends to elongate the KH vortices, thus preventing their rolling. Therefore, the mixing parameter not only provides information about the evolution of the KHI but can also catch the local plasma dynamics suggesting the presence of secondary mechanisms that affect the development of the KH structures.

Furthermore, we statistically investigated such connection between KH properties and local and remote processes with a particular focus on kinetic-scale features like temperature anisotropies and non-local thermal features quantified via the non-Maxwellianity parameter. In agreement with previous observations in the boundary layers, we found that, in the MSH region, ions have a larger temperature anisotropy in the direction perpendicular to the local magnetic field direction (particularly strong during the NKH event), whereas electrons have relatively more isotropic distributions than ions (Hasegawa et al., 2003; Nishino et al., 2007). On the other hand, at the boundary and ceters of KH waves/vortices, electrons have a predominantly (SKH event) or strictly (NKH event) parallel temperature anisotropy. During the SKH event, kinetic quantities at boundaries and center of the KH waves/vortices reach values intermediate between the one in the MSH and MSP sides. Such features suggest that the distortions in the VDFs are likely produced by the mixing and diffusion of two different plasmas. On the contrary, during the NKH event, ion VDFs are highly distorted due to field-aligned beams. The ion non-Maxwellianity also captures these features, since it reaches, at the center of the KH structures, values higher than those at the MSH and MSP sides, thus suggesting the presence of processes different from particle mixing that are accelerating ions.

As a result, thanks to the electron mixing parameter, information about the different properties at the boundaries and center of KH waves/vortices can be recovered and consequently connected to the IMF orientations and other local processes competing with or triggered by the KH instability. The analysis framework we have established in this study can be applied to statistical databases containing events with KH instability at the magnetopause and we envision that similar features can be observed for KH events developing under analogous conditions. However, further analysis are necessary to have a better insight into such interconnection, where numerical kinetic simulations can provide a valid support. Finally, we suggest that the mixing parameter can be used also to investigate other planetary magnetospheres, such as Mercury's magnetopause, for which BepiColombo (Benkhoff et al., 2021) mission can provide both ion and electron VDFs with a resolution close to the typical ion inertial lengths. This would allow to investigate the KH instability in a weak magnetic field environment with an unprecedented resolution.

Acknowledgments

The data used in this paper are freely available from the MMS data center (`https://lasp.colorado.edu/mms/sdc/public/about/browse-wrapper/`). This work was supported by the Austrian Science Fund (FWF): P32175-N27. AS would like to thank Dr D. Perrone for the insightful scientific discussions about the analysis with a particular focus on the local non-thermal features; Dr A. Varsani for the helpful discussion about technical features concerning ion and electron VDFs and finally, Dr M. Simon Wedlund for the precious support and discussion during the development of the manuscript. CSW thanks the Austrian Science Fund (Fonds zur Förderung der wissenschaftlichen Forschung) and FWF project P35954-N.

References

Barrie, A. C., Cipriani, F., Escoubet, C. P., Toledo-Redondo, S., Nakamura, R., Torkar, K., … Schiff, C. (2019, October). Characterizing spacecraft potential effects on measured particle trajectories. *Physics of Plasmas*, *26*(10), 103504.

doi: 10.1063/1.5119344

Benkhoff, J., Murakami, G., Baumjohann, W., Besse, S., Bunce, E., Casale, M., … Zender, J. (2021, December). BepiColombo - Mission Overview and Science Goals. *Soc. Science Res.,*, *217*(8), 90. doi: 10.1007/s11214-021-00861-4

Blasl, K. A., Nakamura, T. K. M., Nakamura, R., Settino, A., Hasegawa, H., Vörös, Z., … Holmes, J. C. (2023, October). Electron-Scale Reconnecting Current Sheet Formed Within the Lower-Hybrid Wave-Active Region of Kelvin-Helmholtz Waves. *Geophys. Res. Lett.,*, *50*(19), e2023GL104309. doi: 10.1029/2023GL104309

Blasl, K. A., Nakamura, T. K. M., Plaschke, F., Nakamura, R., Hasegawa, H., Stawarz, J. E., … Volwerk, M. (2022, January). Multi-scale observations of the magnetopause Kelvin-Helmholtz waves during southward IMF. *Physics of Plasmas*, *29*(1), 012105. doi: 10.1063/5.0067370

Burch, J. L., Moore, T. E., Torbert, R. B., & Giles, B. L. (2016, March). Magnetospheric Multiscale Overview and Science Objectives. *Social Science Research*, *199*(1-4), 5-21. doi: 10.1007/s11214-015-0164-9

Chandrasekhar, S. (1961). *Hydrodynamic and hydromagnetic stability.*

Daughton, W., Nakamura, T. K. M., Karimabadi, H., Roytershteyn, V., & Loring, B. (2014, May). Computing the reconnection rate in turbulent kinetic layers by using electron mixing to identify topology. *Physics of Plasmas*, *21*(5), 052307. doi: 10.1063/1.4875730

Ergun, R. E., Tucker, S., Westfall, J., Goodrich, K. A., Malaspina, D. M., Summers, D., … Cully, C. M. (2016, March). The Axial Double Probe and Fields Signal Processing for the MMS Mission. *Soc. Science Res.,*, *199*(1-4), 167-188. doi: 10.1007/s11214-014-0115-x

Eriksson, S., Lavraud, B., Wilder, F. D., Stawarz, J. E., Giles, B. L., Burch, J. L., … Goodrich, K. A. (2016, June). Magnetospheric Multiscale observations of magnetic reconnection associated with Kelvin-Helmholtz waves. *J. Geophys. Res*, *43*(11), 5606-5615. doi: 10.1002/2016GL068783

Eriksson, S., Ma, X., Burch, J. L., Otto, A., Elkington, S., & Delamere, P. A. (2021, November). MMS Observations of Double Mid-Latitude Reconnection Ion Beams in the Early Non-Linear Phase of the Kelvin-Helmholtz Instability. *Frontiers in Astronomy and Space Sciences*, *8*, 188. doi: 10.3389/fspas.2021.760885

Faganello, M., & Califano, F. (2017, December). Magnetized Kelvin-Helmholtz instability: theory and simulations in the Earth's magnetosphere context. *Journal of Plasma Physics*, *83*(6), 535830601. doi: 10.1017/S0022377817000770

Faganello, M., Califano, F., & Pegoraro, F. (2008, January). Competing Mechanisms of Plasma Transport in Inhomogeneous Configurations with Velocity Shear: The Solar-Wind Interaction with Earth's Magnetosphere. *Physical Review Letter*, *100*(1), 015001. doi: 10.1103/PhysRevLett.100.015001

Fairfield, D. H., Otto, A., Mukai, T., Kokubun, S., Lepping, R. P., Steinberg, J. T., … Yamamoto, T. (2000, September). Geotail observations of the Kelvin-Helmholtz instability at the equatorial magnetotail boundary for parallel northward fields. *J. Geophys. Res.*, *105*(A9), 21,159-21,173.

Foullon, C., Farrugia, C. J., Fazakerley, A. N., Owen, C. J., Gratton, F. T., & Torbert, R. B. (2008, November). Evolution of Kelvin-Helmholtz activity on the dusk flank magnetopause. *Journal of Geophysical Research (Space Physics)*, *113*(A11), A11203. doi: 10.1029/2008JA013175

Gershman, D. J., Avanov, L. A., Boardsen, S. A., Dorelli, J. C., Gliese, U., Barrie, A. C., … Pollock, C. J. (2017, November). Spacecraft and Instrument Photoelectrons Measured by the Dual Electron Spectrometers on MMS. *Journal of Geophysical Research (Space Physics)*, *122*(11), 11,548-11,558. doi: 10.1002/2017JA024518

Graham, D. B., Khotyaintsev, Y. V., André, M., Vaivads, A., Chasapis, A., Matthaeus, W. H., . . . Gershman, D. J. (2021, October). Non-Maxwellianity of Electron Distributions Near Earth's Magnetopause. *Journal of Geophysical Research (Space Physics)*, *126*(10), e29260. doi: 10.1029/2021JA029260

Greco, A., Valentini, F., Servidio, S., & Matthaeus, W. H. (2012, December). Inhomogeneous kinetic effects related to intermittent magnetic discontinuities. *Physical Review E*, *86*(6), 066405. doi: 10.1103/PhysRevE.86.066405

Hasegawa, H., Fujimoto, M., Maezawa, K., Saito, Y., & Mukai, T. (2003, April). Geotail observations of the dayside outer boundary region: Interplanetary magnetic field control and dawn-dusk asymmetry. *Journal of Geophysical Research (Space Physics)*, *108*(A4), 1163. doi: 10.1029/2002JA009667

Hasegawa, H., Fujimoto, M., Phan, T. D., Rème, H., Balogh, A., Dunlop, M. W., . . . TanDokoro, R. (2004, August). Transport of solar wind into Earth's magnetosphere through rolled-up Kelvin-Helmholtz vortices. *Nature*, *430*(7001), 755-758. doi: 10.1038/nature02799

Hasegawa, H., Fujimoto, M., Takagi, K., Saito, Y., Mukai, T., & RèMe, H. (2006, September). Single-spacecraft detection of rolled-up Kelvin-Helmholtz vortices at the flank magnetopause. *Journal of Geophysical Research (Space Physics)*, *111*(A9), A09203. doi: 10.1029/2006JA011728

Henry, Z. W., Nykyri, K., Moore, T. W., Dimmock, A. P., & Ma, X. (2017, December). On the Dawn-Dusk Asymmetry of the Kelvin-Helmholtz Instability Between 2007 and 2013. *Journal of Geophysical Research (Space Physics)*, *122*(12), 11,888-11,900. doi: 10.1002/2017JA024548

Hwang, K. J., Goldstein, M. L., Kuznetsova, M. M., Wang, Y., ViñAs, A. F., & Sibeck, D. G. (2012, August). The first in situ observation of Kelvin-Helmholtz waves at high-latitude magnetopause during strongly dawnward interplanetary magnetic field conditions. *Journal of Geophysical Research (Space Physics)*, *117*(A8), A08233. doi: 10.1029/2011JA017256

Kavosi, S., & Raeder, J. (2015, May). Ubiquity of Kelvin-Helmholtz waves at Earth's magnetopause. *Nature Communications*, *6*, 7019. doi: 10.1038/ncomms8019

Kavosi, S., Raeder, J., Johnson, J. R., Nykyri, K., & Farrugia, C. J. (2023, May). Seasonal and diurnal variations of Kelvin-Helmholtz Instability at terrestrial magnetopause. *Nature Communications*, *14*, 2513. doi: 10.1038/s41467-023-37485-x

Kivelson, M. G., & Chen, S.-H. (1995, January). The magnetopause: Surface waves and instabilities and their possible dynamical consequences. *Washington DC American Geophysical Union Geophysical Monograph Series*, *90*, 257-268. doi: 10.1029/GM090p0257

Li, W., André, M., Khotyaintsev, Y. V., Vaivads, A., Graham, D. B., Toledo-Redondo, S., . . . Strangeway, R. J. (2016, June). Kinetic evidence of magnetic reconnection due to Kelvin-Helmholtz waves. *J. Geophys. Res*, *43*(11), 5635-5643. doi: 10.1002/2016GL069192

Li, W. Y., Guo, X. C., & Wang, C. (2012, August). Spatial distribution of Kelvin-Helmholtz instability at low-latitude boundary layer under different solar wind speed conditions. *Journal of Geophysical Research (Space Physics)*, *117*(A8), A08230. doi: 10.1029/2012JA017780

Lin, D., Wang, C., Li, W., Tang, B., Guo, X., & Peng, Z. (2014, September). Properties of Kelvin-Helmholtz waves at the magnetopause under northward interplanetary magnetic field: Statistical study. *Journal of Geophysical Research (Space Physics)*, *119*(9), 7485-7494. doi: 10.1002/2014JA020379

Lindqvist, P. A., Olsson, G., Torbert, R. B., King, B., Granoff, M., Rau, D., . . . Tucker, S. (2016, March). The Spin-Plane Double Probe Electric Field Instrument for MMS. *Soc. Science Res.,*, *199*(1-4), 137-165. doi: 10.1007/s11214-014-0116-9

Ma, X., Delamere, P., Nykyri, K., Burkholder, B., Eriksson, S., & Liou, Y.-L. (2021, November). Ion dynamics in the meso-scale 3-D Kelvin-Helmholtz instability: perspectives from test particle simulations. *Frontiers in Astronomy and Space Sciences*, *8*, 185. doi: 10.3389/fspas.2021.758442

Ma, X., Otto, A., & Delamere, P. A. (2014a, February). Interaction of magnetic reconnection and Kelvin-Helmholtz modes for large magnetic shear: 1. Kelvin-Helmholtz trigger. *Journal of Geophysical Research (Space Physics)*, *119*(2), 781-797. doi: 10.1002/2013JA019224

Ma, X., Otto, A., & Delamere, P. A. (2014b, February). Interaction of magnetic reconnection and Kelvin-Helmholtz modes for large magnetic shear: 2. Reconnection trigger. *Journal of Geophysical Research (Space Physics)*, *119*(2), 808-820. doi: 10.1002/2013JA019225

Matsumoto, Y., & Hoshino, M. (2004, January). Onset of turbulence induced by a Kelvin-Helmholtz vortex. *J. Geophys. Res*, *31*(2), L02807. doi: 10.1029/2003GL018195

Miura, A. (1982, September). Nonlinear evolution of the magnetohydrodynamic Kelvin-Helmholtz instability. *Physical Review Letter*, *49*(11), 779-782. doi: 10.1103/PhysRevLett.49.779

Nakamura, T. K. M. (2021, May). The Earths Low-Latitude Boundary Layer. In R. Maggiolo, N. André, H. Hasegawa, & D. T. Welling (Eds.), *Magnetospheres in the solar system* (Vol. 2, p. 177). doi: 10.1002/9781119815624.ch12

Nakamura, T. K. M., Blasl, K. A., Hasegawa, H., Umeda, T., Liu, Y. H., Peery, S. A., ... Nystrom, W. D. (2022, January). Multi-scale evolution of Kelvin-Helmholtz waves at the Earth's magnetopause during southward IMF periods. *Physics of Plasmas*, *29*(1), 012901. doi: 10.1063/5.0067391

Nakamura, T. K. M., Hasegawa, H., Daughton, W., Eriksson, S., Li, W. Y., & Nakamura, R. (2017, November). Turbulent mass transfer caused by vortex induced reconnection in collisionless magnetospheric plasmas. *Nature Communications*, *8*, 1582. doi: 10.1038/s41467-017-01579-0

Nakamura, T. K. M., Plaschke, F., Hasegawa, H., Liu, Y. H., Hwang, K. J., Blasl, K. A., & Nakamura, R. (2020, July). Decay of Kelvin-Helmholtz Vortices at the Earth's Magnetopause Under Pure Southward IMF Conditions. *Geophys. Res. Lett.,*, *47*(13), e87574. doi: 10.1029/2020GL087574

Nishino, M. N., Fujimoto, M., Terasawa, T., Ueno, G., Maezawa, K., Mukai, T., & Saito, Y. (2007, June). Temperature anisotropies of electrons and two-component protons in the dusk plasma sheet. *Annales Geophysicae*, *25*(6), 1417-1432. doi: 10.5194/angeo-25-1417-2007

Nykyri, K. (2013, August). Impact of MHD shock physics on magnetosheath asymmetry and Kelvin-Helmholtz instability. *Journal of Geophysical Research (Space Physics)*, *118*(8), 5068-5081. doi: 10.1002/jgra.50499

Nykyri, K., & Dimmock, A. P. (2016, July). Statistical study of the ULF Pc4-Pc5 range fluctuations in the vicinity of Earth's magnetopause and correlation with the Low Latitude Boundary Layer thickness. *Advances in Space Research*, *58*(2), 257-267. doi: 10.1016/j.asr.2015.12.046

Nykyri, K., & Otto, A. (2001, January). Plasma transport at the magnetospheric boundary due to reconnection in Kelvin-Helmholtz vortices. *J. Geophys. Res*, *28*(18), 3565-3568. doi: 10.1029/2001GL013239

Nykyri, K., Otto, A., Lavraud, B., Mouikis, C., Kistler, L. M., Balogh, A., & Rème, H. (2006, October). Cluster observations of reconnection due to the Kelvin-Helmholtz instability at the dawnside magnetospheric flank. *Annales Geophysicae*, *24*(10), 2619-2643. doi: 10.5194/angeo-24-2619-2006

Otto, A., & Fairfield, D. H. (2000, September). Kelvin-Helmholtz instability at the magnetotail boundary: MHD simulation and comparison with Geotail observations. *J. Geophys. Res.*, *105*(A9), 21,175-21,190. doi: 10.1029/1999JA000312

Perrone, D., Dendy, R. O., Furno, I., Sanchez, R., Zimbardo, G., Bovet, A., ... Valentini, F. (2013, October). Nonclassical Transport and Particle-Field

Coupling: from Laboratory Plasmas to the Solar Wind. *Soc. Science Res.,*, *178*(2-4), 233-270. doi: 10.1007/s11214-013-9966-9

Pollock, C., Moore, T., Jacques, A., Burch, J., Gliese, U., Saito, Y., … Zeuch, M. (2016, March). Fast Plasma Investigation for Magnetospheric Multiscale. *Social Science Research*, *199*(1-4), 331-406. doi: 10.1007/s11214-016-0245-4

Russell, C. T., Anderson, B. J., Baumjohann, W., Bromund, K. R., Dearborn, D., Fischer, D., … Richter, I. (2016, March). The Magnetospheric Multiscale Magnetometers. *Social Science Research*, *199*(1-4), 189-256. doi: 10.1007/s11214-014-0057-3

Servidio, S., Valentini, F., Califano, F., & Veltri, P. (2012, January). Local Kinetic Effects in Two-Dimensional Plasma Turbulence. *Phys. Rev. Lett.,*, *108*(4), 045001. doi: 10.1103/PhysRevLett.108.045001

Settino, A., Khotyaintsev, Y. V., Graham, D. B., Perrone, D., & Valentini, F. (2022, February). Characterizing Satellite Path Through Kelvin-Helmholtz Instability Using a Mixing Parameter. *Journal of Geophysical Research (Space Physics)*, *127*(2), e2021JA029758. doi: 10.1029/2021JA029758

Settino, A., Malara, F., Pezzi, O., Onofri, M., Perrone, D., & Valentini, F. (2020, September). Kelvin-Helmholtz Instability at Proton Scales with an Exact Kinetic Equilibrium. *The Astrophysical Journal*, *901*(1), 17. doi: 10.3847/1538-4357/abada9

Settino, A., Perrone, D., Khotyaintsev, Y. V., Graham, D. B., & Valentini, F. (2021, May). Kinetic Features for the Identification of Kelvin-Helmholtz Vortices in In Situ Observations. *The Astrophysical Journal*, *912*(2), 154. doi: 10.3847/1538-4357/abf1f5

Sorriso-Valvo, L., Catapano, F., Retinò, A. r., Le Contel, O., Perrone, D., Roberts, O. W., … Khotyaintsev, Y. V. (2019, January). Turbulence-Driven Ion Beams in the Magnetospheric Kelvin-Helmholtz Instability. *Physical Review Letter*, *122*(3), 035102. doi: 10.1103/PhysRevLett.122.035102

Stawarz, J. E., Eriksson, S., Wilder, F. D., Ergun, R. E., Schwartz, S. J., Pouquet, A., … Sturner, A. P. (2016, November). Observations of turbulence in a Kelvin-Helmholtz event on 8 September 2015 by the Magnetospheric Multiscale mission. *Journal of Geophysical Research (Space Physics)*, *121*(11), 11,021-11,034. doi: 10.1002/2016JA023458

Swisdak, M. (2016, January). Quantifying gyrotropy in magnetic reconnection. *J. Geophys. Res*, *43*(1), 43-49. doi: 10.1002/2015GL066980

Torkar, K., Nakamura, R., Tajmar, M., Scharlemann, C., Jeszenszky, H., Laky, G., … Svenes, K. (2016, March). Active Spacecraft Potential Control Investigation. *Soc. Science Res.,*, *199*(1-4), 515-544. doi: 10.1007/s11214-014-0049-3

Valentini, F., Perrone, D., Stabile, S., Pezzi, O., Servidio, S., De Marco, R., … Veltri, P. (2016, December). Differential kinetic dynamics and heating of ions in the turbulent solar wind. *New Journal of Physics*, *18*(12), 125001. doi: 10.1088/1367-2630/18/12/125001

Vernisse, Y., Lavraud, B., Eriksson, S., Gershman, D. J., Dorelli, J., Pollock, C., … Yokota, S. (2016, October). Signatures of complex magnetic topologies from multiple reconnection sites induced by Kelvin-Helmholtz instability. *Journal of Geophysical Research (Space Physics)*, *121*(10), 9926-9939. doi: 10.1002/2016JA023051

Figure1.

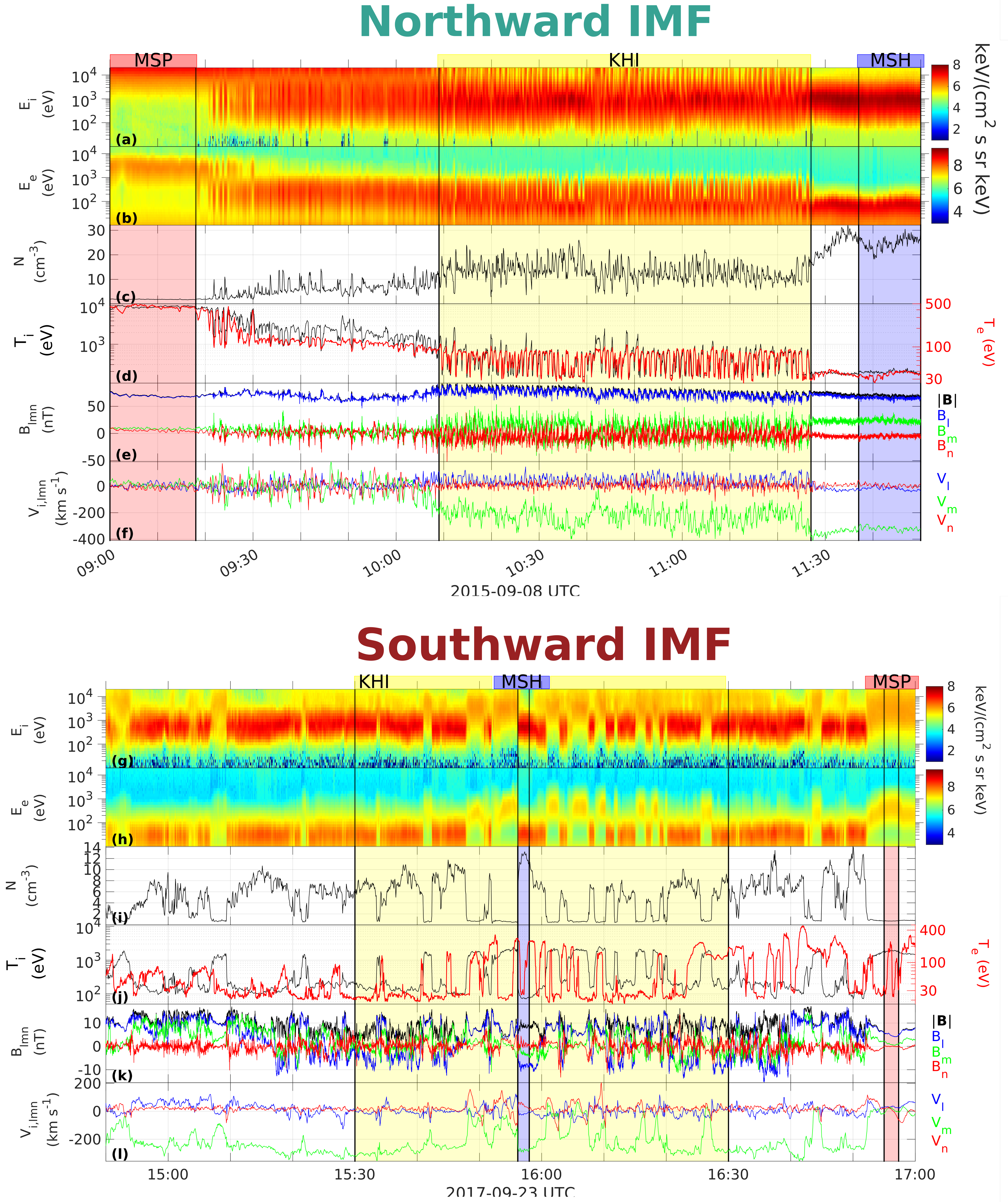

Northward IMF
MSP
KHI
MSH
(a)
(b)
(c)
(d)
(e)
(f)
2015-09-08 UTC
Southward IMF
KHI
MSH
MSP
(g)
(h)
(i)
(j)
(k)
(l)
2017-09-23 UTC

Figure2a.

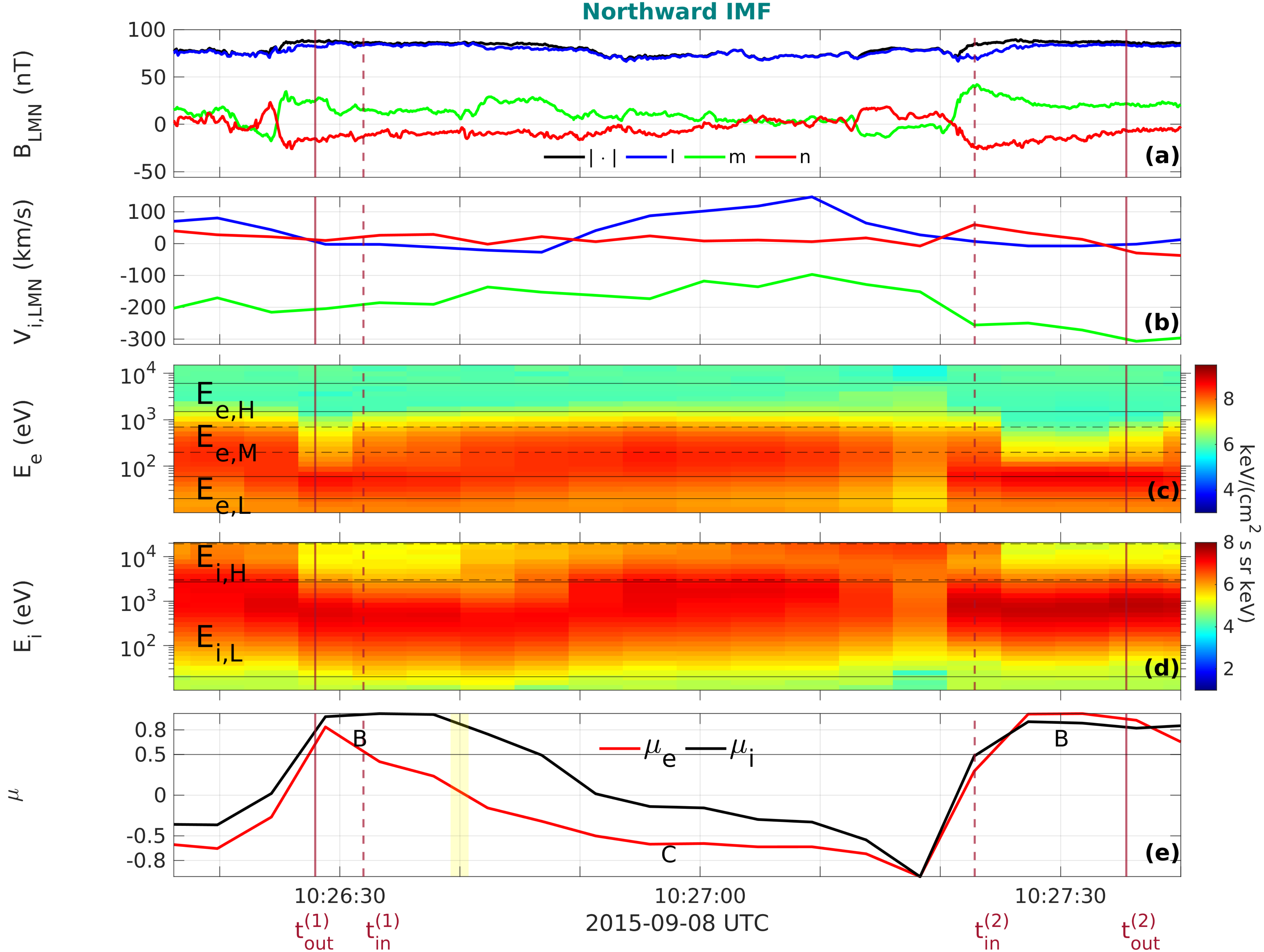

Northward IMF
B_LMN (nT)
| · |
l
m
n
(a)
V_i,LMN (km/s)
(b)
E_e (eV)
E_e,H
E_e,M
E_e,L
(c)
keV/(cm^2 s sr keV)
E_i (eV)
E_i,H
E_i,L
(d)
μ
μ_e
μ_i
B
C
B
(e)
10:26:30
10:27:00
10:27:30
2015-09-08 UTC
t_out^(1)
t_in^(1)
t_in^(2)
t_out^(2)

Figure2b.

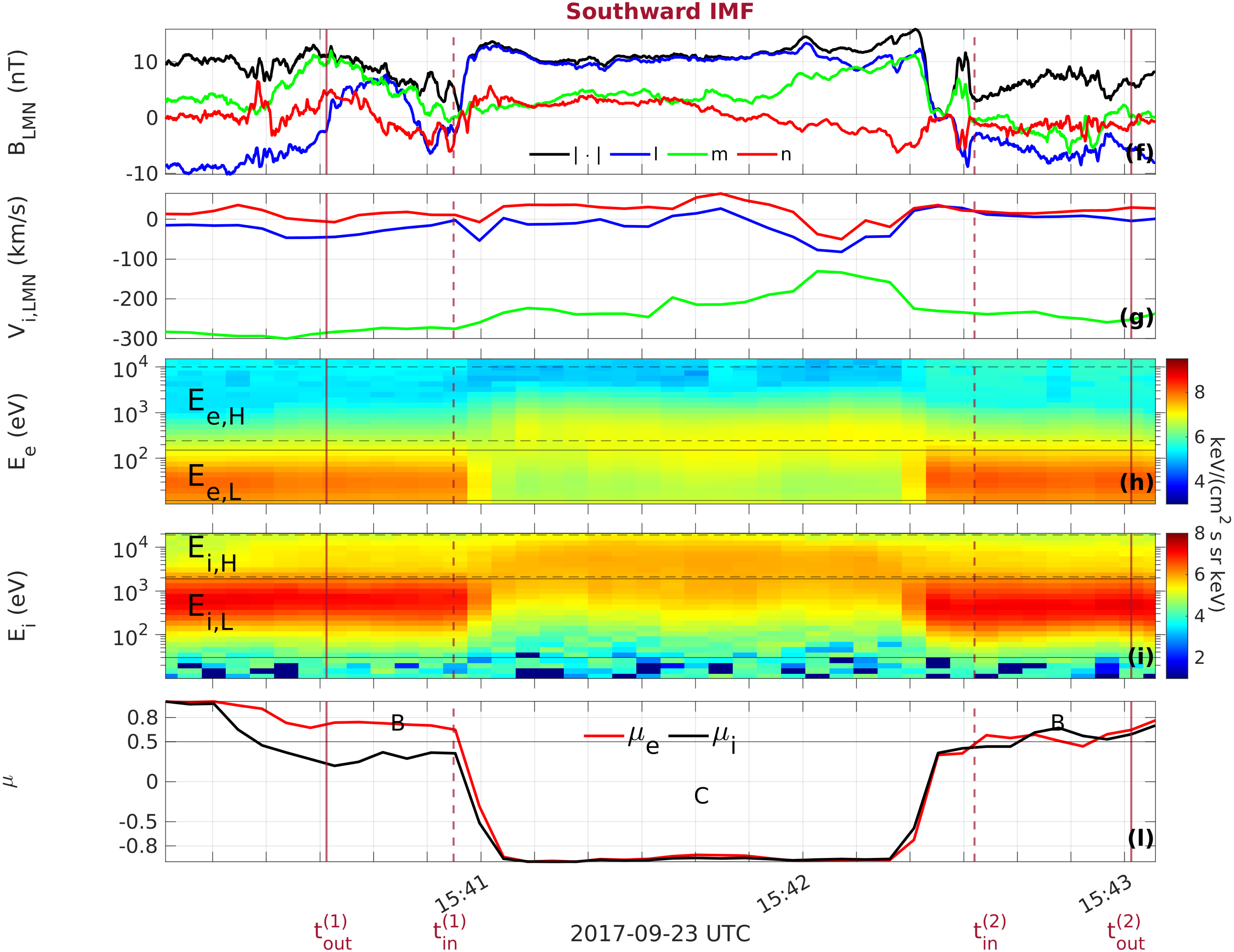

Southward IMF
B_LMN (nT)
|·|
l
m
n
(f)
V_i,LMN (km/s)
(g)
E_e (eV)
E_e,H
E_e,L
(h)
keV/(cm^2 s sr keV)
E_i (eV)
E_i,H
E_i,L
(i)
μ
B
C
μ_e
μ_i
(l)
15:41
15:42
15:43
2017-09-23 UTC
t_out^(1)
t_in^(1)
t_in^(2)
t_out^(2)

Figure3.

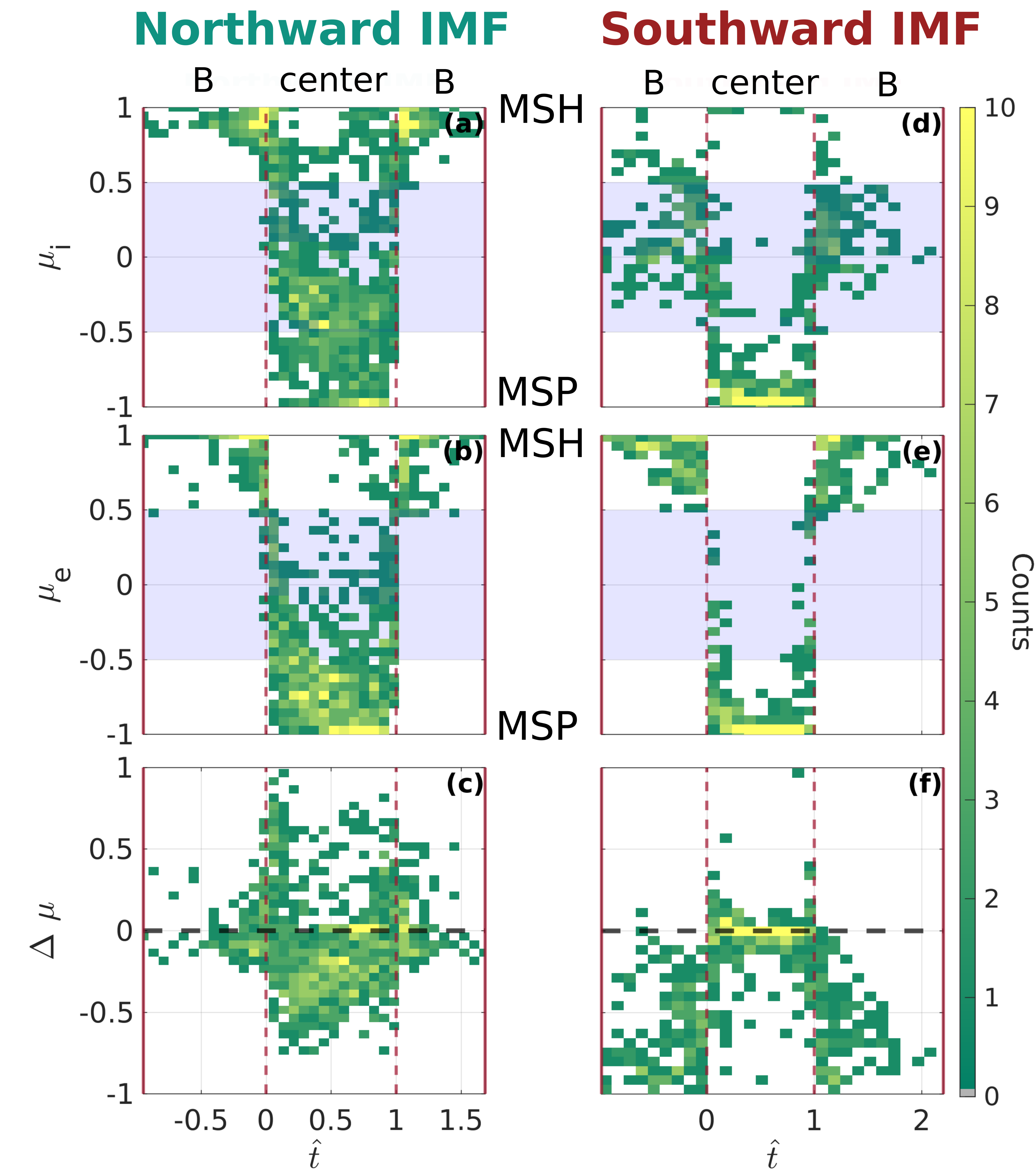

Northward IMF
Southward IMF
B
center
B
MSH
MSP
(a)
(b)
(c)
(d)
(e)
(f)
μ_i
μ_e
$\Delta\mu$
$\hat{t}$
Counts

Figure4.

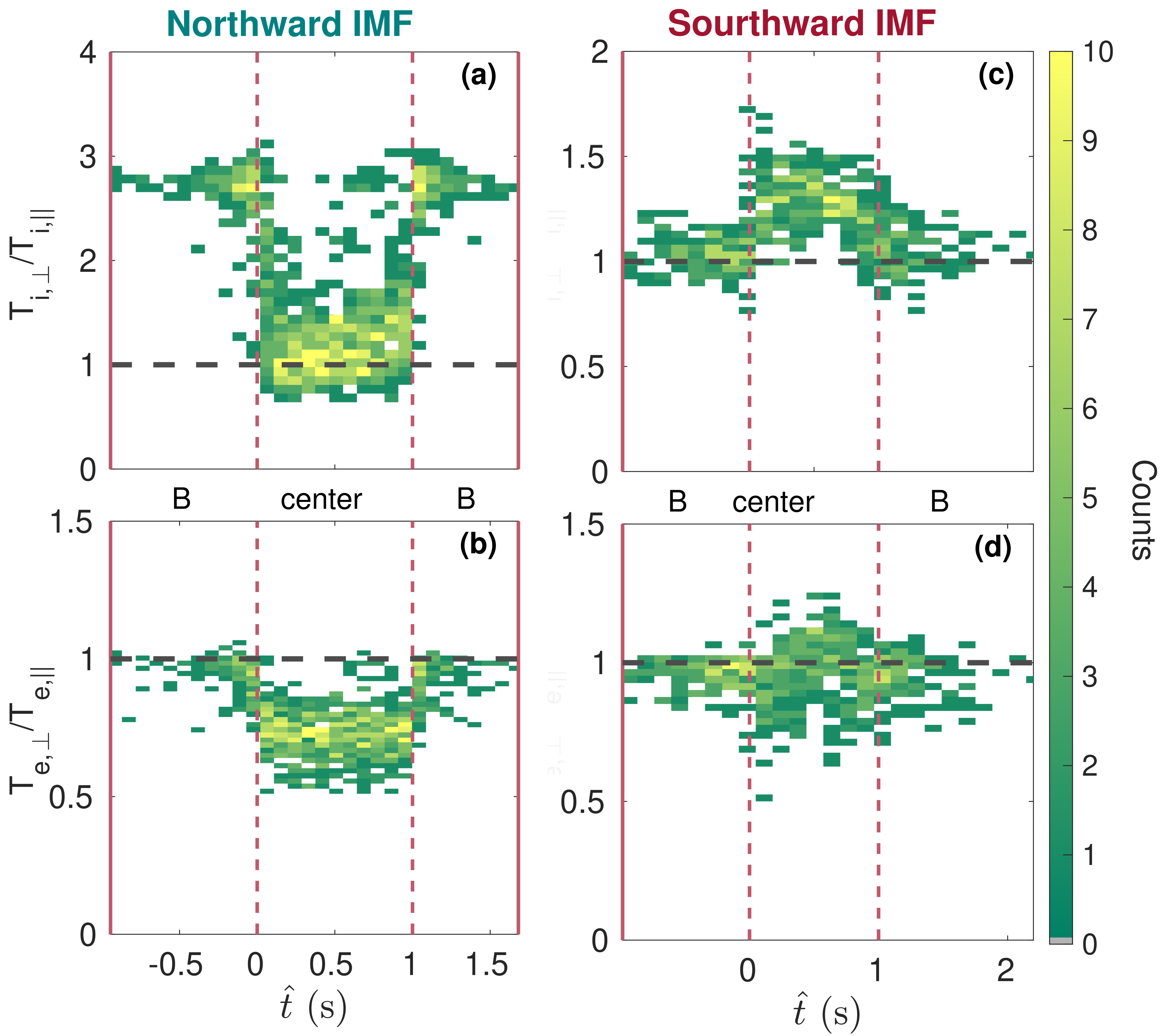

Northward IMF
Sourthward IMF
(a)
(b)
(c)
(d)
$T_{i,\perp}/T_{i,||}$
$T_{e,\perp}/T_{e,||}$
B
center
B
B
center
B
$\hat{t}$ (s)
$\hat{t}$ (s)
Counts

Figure5.

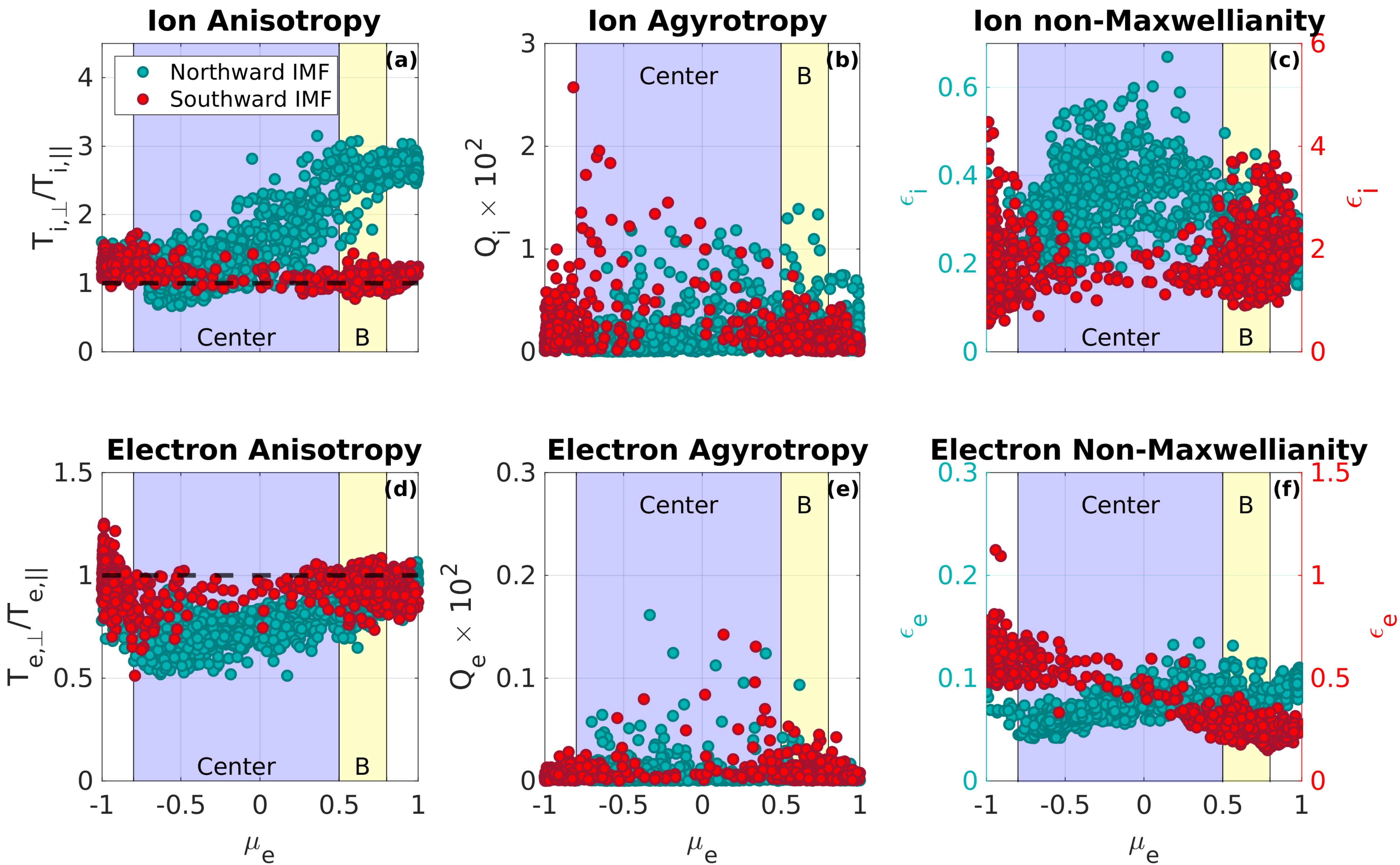
Ion Anisotropy
Ion Agyrotropy
Ion non-Maxwellianity
Electron Anisotropy
Electron Agyrotropy
Electron Non-Maxwellianity
Northward IMF
Southward IMF
(a)
(b)
(c)
(d)
(e)
(f)
Center
B
$T_{i,\perp}/T_{i,||}$
$Q_i \times 10^2$
ϵ_i
$T_{e,\perp}/T_{e,||}$
$Q_e \times 10^2$
ϵ_e
μ_e

Figure6.

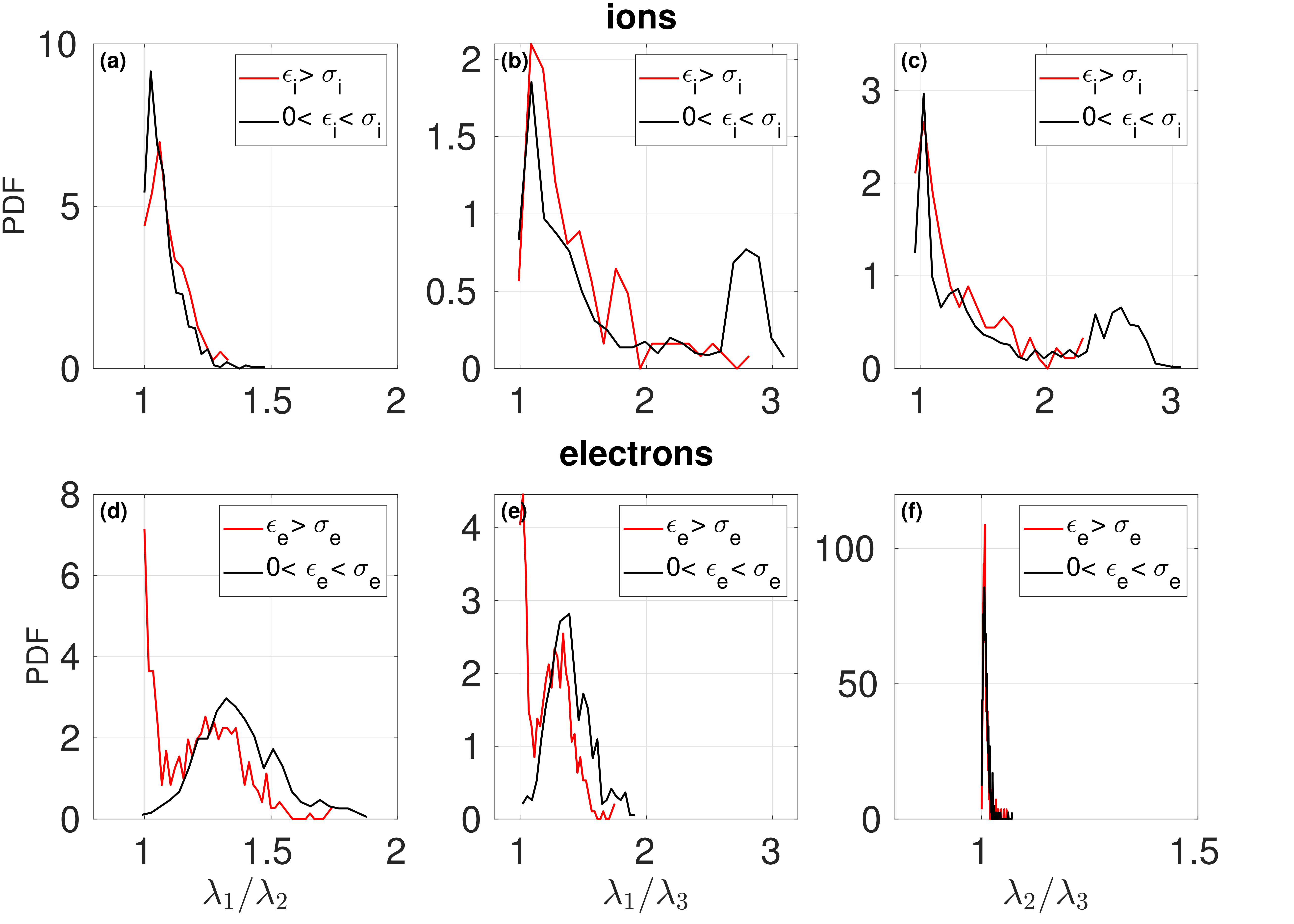
ions
electrons
PDF
PDF
(a)
(b)
(c)
(d)
(e)
(f)
$\epsilon_i > \sigma_i$
$0 < \epsilon_i < \sigma_i$
$\epsilon_e > \sigma_e$
$0 < \epsilon_e < \sigma_e$
λ_1/λ_2
λ_1/λ_3
λ_2/λ_3

Figure7a.

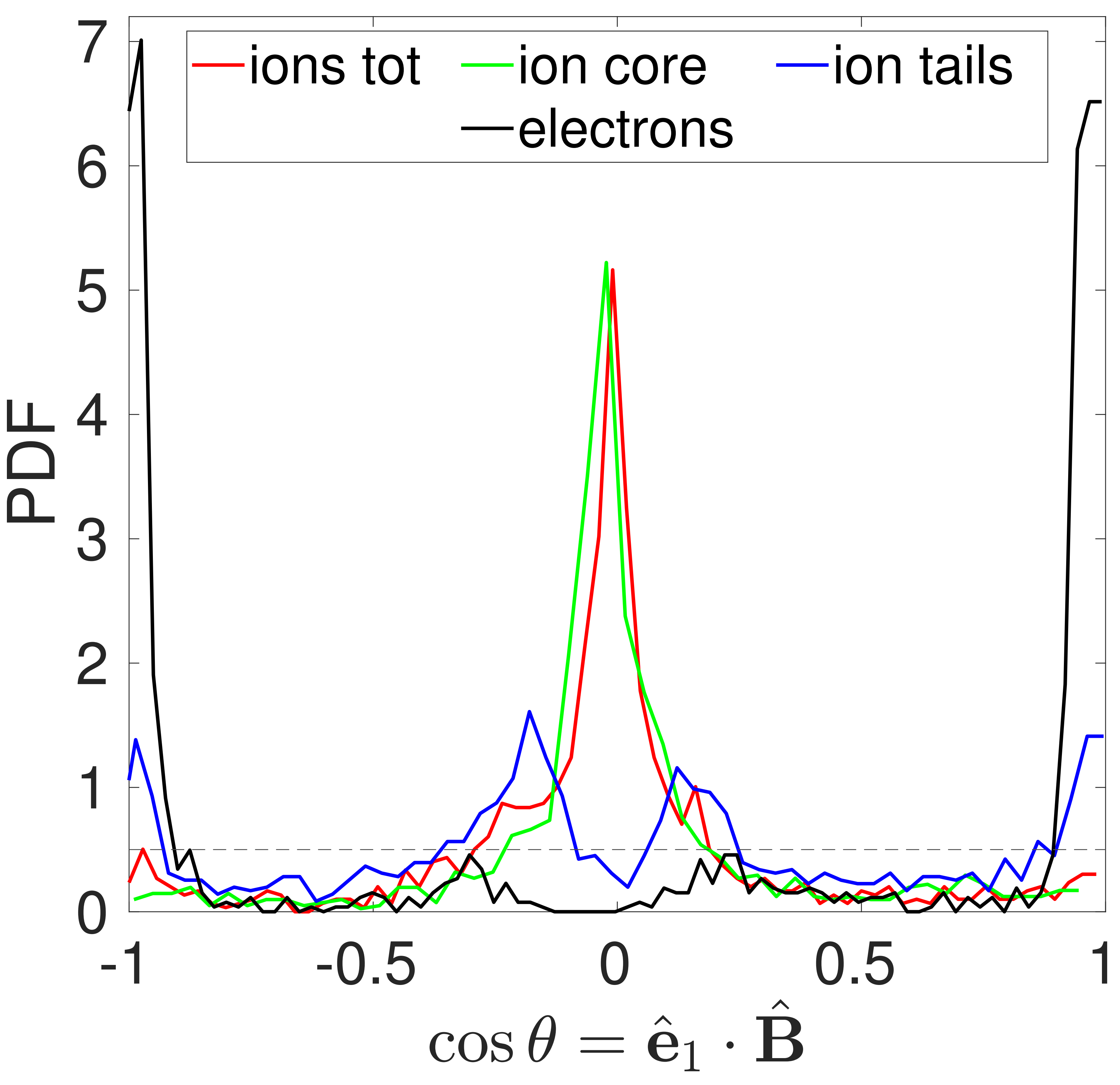

ions tot
ion core
ion tails
electrons
PDF
0
1
2
3
4
5
6
7
-1
-0.5
0
0.5
1
$\cos\theta = \hat{\mathbf{e}}_1 \cdot \hat{\mathbf{B}}$

Figure7b.

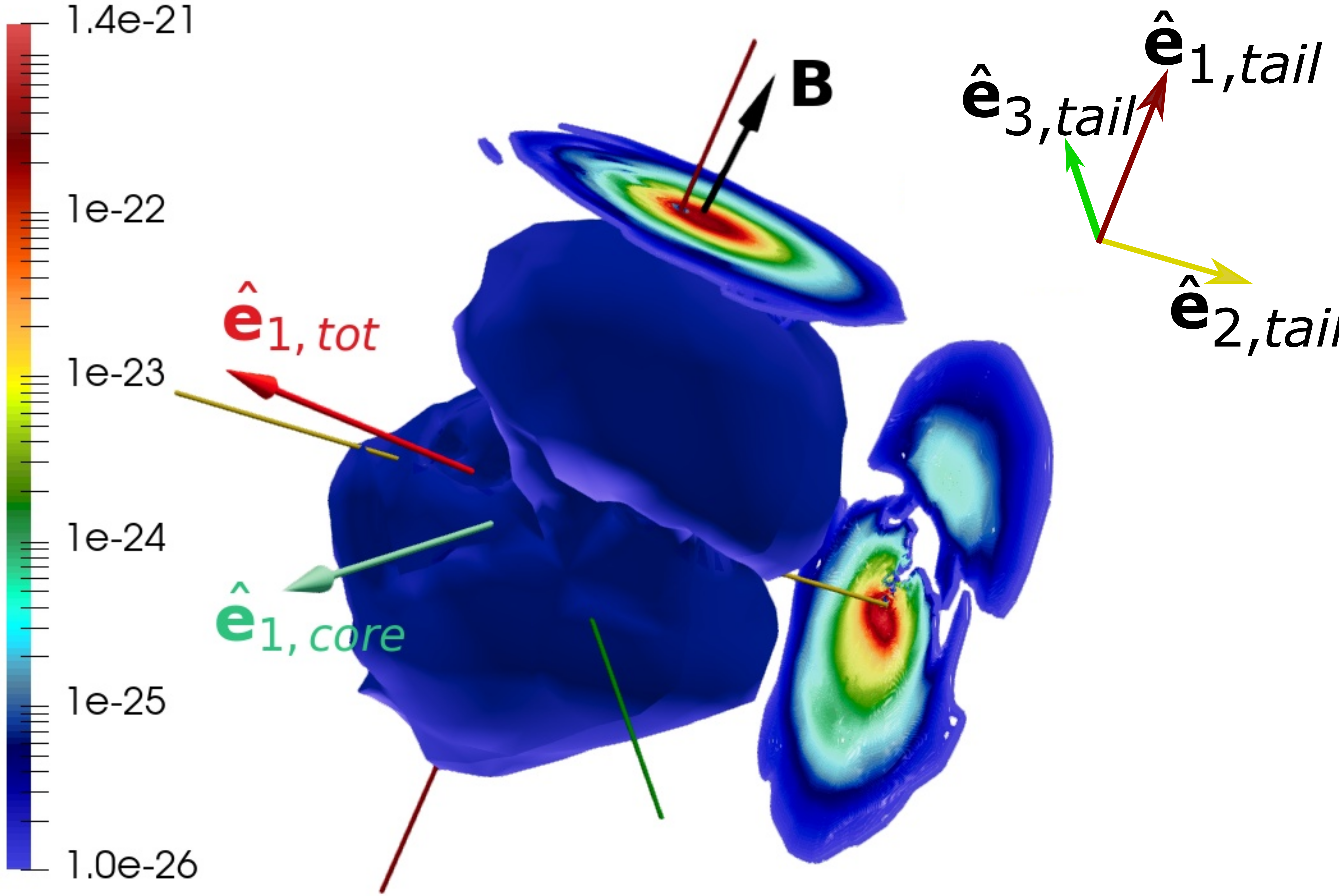
1.4e-21
1e-22
1e-23
1e-24
1e-25
1.0e-26
B
$\hat{\mathbf{e}}_{1,tail}$
$\hat{\mathbf{e}}_{3,tail}$
$\hat{\mathbf{e}}_{2,tail}$
$\hat{\mathbf{e}}_{1,tot}$
$\hat{\mathbf{e}}_{1,core}$